Nonlinear functionally graded metamaterials for hydrogen storage and enhanced sustainability under extreme environments

Article *in* Thin-Walled Structures · December 2024

DOI: 10.1016/j.tws.2024.112901

CITATIONS
0

READS
201

3 authors:

Pratik Tiwari
Thapar Institute of Engineering & Technology
15 PUBLICATIONS **87** CITATIONS
SEE PROFILE

Susmita Naskar
University of Southampton
112 PUBLICATIONS **1,209** CITATIONS
SEE PROFILE

Tanmoy Mukhopadhyay
University of Southampton
273 PUBLICATIONS **5,637** CITATIONS
SEE PROFILE

Nonlinear functionally graded metamaterials for hydrogen storage and enhanced sustainability under extreme environments

P. Tiwari[a,b], *S.Naskar*[c], *T.Mukhopadhyay*[c,*]

[a]*Department of Aerospace Engineering, Indian Institute of Technology Kanpur, Kanpur, India*
[b]*Department of Civil Engineering, Thapar Institute of Engineering and Technology, Patiala, India*
[c]*School of Engineering, University of Southampton, Southampton, UK*

Abstract

Functionally graded materials can exhibit remarkable tolerance towards extreme hot or cold environments and chemical surface degradation. This article exploits such properties of functionally graded materials to propose a new class of transversely curved metamaterial architectures with high specific stiffness for operations under extreme surrounding conditions. We envisage the next-generation concept design of hydrogen storage tanks with functionally graded metamaterial core for aerospace and automotive applications. Based on such innovative lattice metamaterial based design of hydrogen storage tanks it is possible to enhance the storage capability in terms of internal pressure and resistance to external loads and impacts. Most importantly the proposed concept would lead to a breakthrough in developing load-bearing energy storage devices. For the metamaterial core, hexagonal bending-dominated unit cell architecture with transversely curved connecting beam-like geometries would ensure the dual functionality of high specific stiffness and energy absorption capability which are mutually exclusive in traditional lattice metamaterials. The functionally graded beams, a periodic network of which constitutes the lattice, are modelled here using 3D degenerated shell elements in a finite element framework. Geometric nonlinearity using Green-Lagrange strain tensor is considered for an accurate analysis. The beam-level nonlinear deformation physics is integrated with the unit cell mechanics following a semi-analytical framework to obtain the effective in-plane and out-of-plane elastic moduli of the metamaterials. The numerical results show that the curved beam lattice metamaterials have significantly enhanced in-plane elastic properties than straight lattices along with a reduced disparity among the in-plane and out-of-plane elastic moduli.

Keywords: Functionally graded metamaterials; Metamaterials for hydrogen storage; Extreme environment metamaterials; Degenerated shells; Sustainable metamaterials; Curved metamaterials

1. Introduction

With the ever growing concern about environmental impacts and climate issues, the urgent necessity to minimize carbon emissions is realized across the countries. In such context of net-zero ambitions, hydrogen as an alternate clean fuel has been attracting significant attention from the aerospace and mechanical industries [1, 2]. However, the storage of hydrogen is a major challenge due to hydrogen

*Corresponding author: T. Mukhopadhyay (Email address: T.Mukhopadhyay@soton.ac.uk)

embitterment, followed by reduced ductility, fracture toughness, strength and fatigue crack growth resistance in the container material. Further hydrogen storage tanks need to sustain significant amount of internal pressure along with external loads and impact, leading to the possibilities of catastrophic failure. Such concerns restrict the industrial adoption and commercialization prospects of hydrogen energy severely. The central theme of this paper is to propose a novel concept of hydrogen storage tanks with metamaterial core for significantly enhanced chemo-mechanical performance and storage capacity.

Hydrogen storage tanks are critical for advancing hydrogen as a clean energy carrier, with research focusing on enhancing their safety, efficiency, and capacity. Conventional storage technologies include compressed hydrogen tanks, liquid hydrogen tanks, and solid-state storage using metal hydrides. Compressed tanks store hydrogen under high pressure (350-700 bar), but challenges like high energy requirements for compression and safety concerns persist [3]. Liquid hydrogen storage offers higher volumetric efficiency but demands cryogenic temperatures (20K), leading to significant energy losses during cooling and boil-off [4]. Solid-state storage materials, such as metal hydrides, provide safer and more compact options but suffer from issues like low hydrogen absorption/desorption kinetics and high weight [5]. This article focuses on improving the storage capacity of hydrogen tanks in terms of internal pressure along with safety issues concerning resistance to external loading.

Lattice metamaterials [6] are a type of artificially engineered materials that possess customized effective material properties suitable for technologically-demanding applications. These metamaterials derive their unique characteristics not only from their intrinsic material properties but also from the geometric arrangement of constituent unit cells. As a result, it becomes possible to modify and fine-tune the material properties of these metamaterials according to the requirements of various applications, enabling the creation of innovative materials with distinct functionalities [7, 8, 9, 10, 11, 12]. Due to their exceptional specific stiffness, strength and energy absorption capability, lightweight metamaterials find extensive applications in various engineering fields [13, 14, 15, 16, 17]. In recent years, engineers and material scientists have focused significantly on the development of complex multi-functional metamaterial architectures, primarily driven by the remarkable progress in the fields of additive manufacturing and material fabrication techniques [18, 19, 20, 21, 22]. The material properties of artificially engineered metamaterials are noticeably different from the intrinsic properties of the constituent materials (i.e. material of the connecting beams) of the lattice structure. In traditional design of metamaterials isotropic intrinsic materials are used that would not be suitable for catering extreme surrounding environments (very high or low temperature, adverse chemicals etc.) such as marine and space. Further, traditional metamaterials with isotropic intrinsic materials cannot be used where the connecting beams may come

in contact with liquids and gases that may chemically react with the beam material, resulting in material property degradation. In this article, we would propose a novel class of functionally graded lattices where the outer surfaces of the constituting beams are made of inert ceramic materials, while the beam cross-section becomes metal-rich near to the center (refer to Figure 1(h)). This will allow lattices to be used under extreme surrounding environments while maintaining adequate mechanical properties.

A significant surge in the research investigations concerning mechanical metamaterials can be noticed over the last decade, primarily driven by the growing need for multi-functional and extreme-property materials that cannot be achieved through traditional naturally occurring substances. An extensive literature review has shown that honeycomb lattice metamaterials exhibit a superior strength-weight ratio and possess exceptional capability in modulating multiple mechanical properties. As a result, different bending and stretching dominated honeycomb lattice metamaterials have gathered substantial attention and interest for a range of structural demands such as specific stiffness, strength and Poisson's ratios [23, 24, 25, 26, 27, 28, 29, 30]. The majority of these studies focus on analyzing the effective material properties by examining a single unit cell with appropriate boundary condition due to the periodic nature of the lattice geometry [31]. Besides analyzing effective elastic properties, considerable focus has been placed on investigating the mechanical response of honeycomb structures under various conditions such as buckling, crushing, and impact [32, 33, 34, 35, 36, 37, 38, 39]. The advances in additive manufacturing techniques have expanded the scope of research in metamaterial design to encompass lattices composed of multiple intrinsic materials [40, 41, 42, 43, 44]. Recent studies have analytically examined the physics of irregularity and disorder in lattices, noting that irregularities in lattice metamaterials can originate from factors such as pre-stressing, microstructural flaws, and manufacturing uncertainties [45, 46, 47]. The concept of anti-curvature and transversely-curved geometries have been proposed in the context of bi-level metamaterial design (involving coupled unit cell and beam-level architectures) for enhancing the effective elastic moduli [48, 49, 50] and failure strength [51]. The bi-level metamaterial design concepts have recently been extended further to propose active and inflatable lattices to achieve on-demand modulation of effective elastic moduli and shape morphing [52, 53, 54, 55, 56]. Traditionally the connecting beam-like elements in the above lattice metamaterials are made of isotropic materials, except for a recently proposed study on composite lattices [50]. Laminated composites, as conceived to be the architecture of the constituting beams in the lattice, represent a distinct category of artificially engineered materials that offer the advantage of tailoring material properties through adjustments in ply orientation within the laminate structure. These composites possess lightweight characteristics and exhibit superior strength compared to isotropic materials [57]. Although composite materials offer vari-

ous benefits over metallic structures, they are prone to issues such as delamination, matrix cracking, and matrix-fiber debonding [58]. To address these challenges, functionally graded materials (FGMs) have emerged as a viable solution. FGMs are a specialized type of composite material, typically composed of a mixture of metal and ceramic in specific volume ratios. In particular, the material properties of FGMs gradually vary throughout the thickness, ensuring a smooth transition from one surface to the other [59, 60]. Initially developed for their remarkable thermal barrier properties, FGM beams, plates and shell structures have proven to be an effective solution for a range of adverse surrounding conditions [61, 62, 63, 64]. Recently functionally graded nonlinear lattices have been developed considering gradation along the length of the cell walls, leading to a unique capability of failure mode manipulation (brittle and ductile) along with stiffness modulation [65]. In this work, we aim to introduce FGM beam-like elements with thickness-wise gradation (refer to Figure 1(f, h)) to form the unit cells (refer to Figure 1(d)) and the lattice metamaterials (refer to Figure 1(a)) with the ambition of using these advanced materials in adverse surroundings such as extreme temperature or environments prone to chemical material degradation.

From the concise literature review on lattice metamaterials presented above, it can be gathered than normally bending dominated lattice geometries such as hexagonal lattices can absorb high amount of energy under impact, while they show relatively lower specific stiffness compared to stretching dominated lattice geometries such as rectangular or triangular lattices. In most of the mechanical and aerospace applications, high specific stiffness is normally desirable along with high specific energy absorption capability. We propose to achieve such conventionally mutually exclusive dual functionality here by exploiting the deformation physics of unit cells which are derived from the deformation of the constituting beam-like elements. A transverse curvature (refer to Figure 1(f)) would be introduced in the constituting beam elements to enhance the bending stiffness of these members substantially, which will result in reduced deformation of the unit cells under applied far-field stresses. This will lead to enhanced specific stiffness of the lattice metamaterials without any appreciable increment of weight. For nonlinear finite element modeling of the beam-like elements, accurate degenerated shell elements [66, 67, 68, 69, 70, 71, 72, 73, 74, 75] will be exploited (refer to Figure 1(e)), and subsequently the beam-level numerical results will be integrated with unit cell mechanics following a nonlinear semi-analytical framework to obtain the effective elastic properties of the lattices.

Based on the literature review, it is evident that no previous studies have focused on the development of metamaterials specifically designed for extreme surrounding environments. Our research aims to leverage the behavior of curved beams to achieve mutually exclusive dual functionality of high specific

stiffness and high energy absorption capability in metamaterials, while making theme suitable for adverse surroundings by introducing functionally graded materials. The outer sides of the proposed constituting beams are rich in ceramic to shield the structure from extreme surrounding environmental effects, while the center part of the beam is rich in metal to enhance strength and stiffness. We would develop an accurate semi-analytical framework for investigating the nonlinear large-deformation response and effective elastic moduli (all in-plane and out-of-plane mouduli, leading to characterization of the entire 3D constitutive matrix) of the proposed functionally graded lattices considering non-auxetic and auxetic unit cell geometries (refer to Figure 1(a, b)). The primarily focus will be placed on proposing a novel class of futuristic hydrogen storage tanks with enhanced mechanical performance and storage capacity, where the functionally graded metamaterials would be used as a core, as depicted in 1(i). In the following sections, after providing a brief description of the concept design of metamaterial-core hydrogen storage tank, we present the detailed mathematical formulation for predicting the effective nonlinear elastic moduli of the lattice metamaterials. Subsequent sections comprise of comprehensive numerical results on the in-plane and out-of-plane elastic properties of the proposed metamaterial, followed by concluding remarks.

2. Metamaterial based design concepts for load-bearing hydrogen storage tanks

Storage of hydrogen is a major challenge due to hydrogen embitterment, followed by reduced ductility, fracture toughness, strength and fatigue crack growth resistance in the container material. Further hydrogen storage tanks need to sustain significant amount of internal pressure along with external loads and impact, leading to the possibilities of catastrophic failure. The central theme of this paper is to propose a novel concept of hydrogen storage tanks with metamaterial core (refer to Figure 1(i)) for significantly enhanced chemo-mechanical performance and storage capacity. The introduction of metamaterial core in the storage tank will mechanically strengthen it for accommodating more internal hydrogen pressure, leading to enhanced storage capacity. Further the resistance to external loads and impact would be improved by orders of magnitude compared to hollow circular cylindrical structures. By introducing bending dominated hexagonal architectures (refer to Figure 1(a, b, i(I))) as the metamaterial core with transversely curved beam-like elements (refer to Figure 1(f)), we ensure the dual functionality of high impact energy absorption capability and high specific stiffness and strength. In Figure 2(h, i), a simple illustration is provided as to how the introduction of transverse curvature can increase the bending stiffness of the cell walls significantly. A similar effect would be exploited through the beam-like cell walls of the honeycombs. Further the motion-induced dynamic instability in the liquid hydrogen

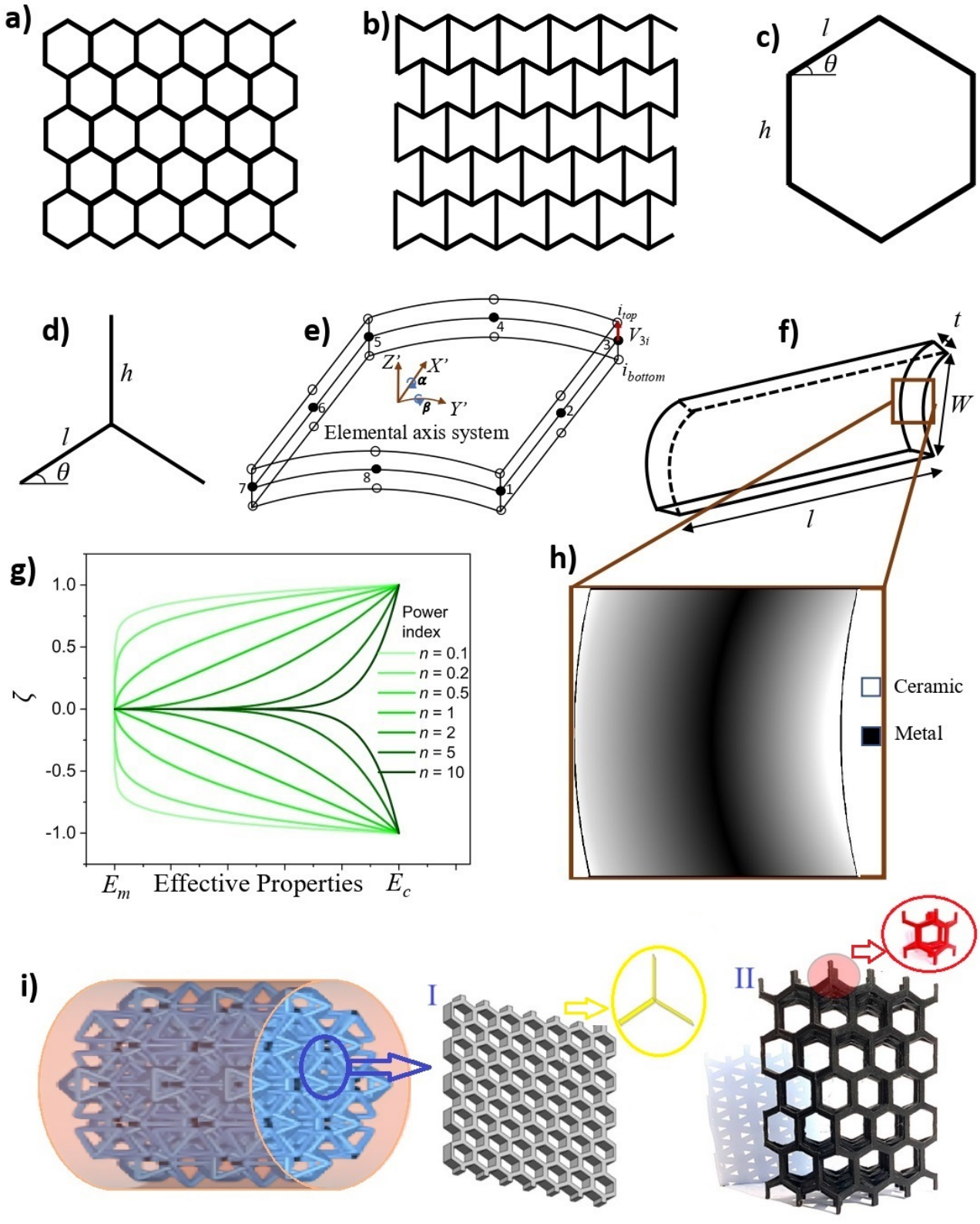

Figure 1: Functionally graded metamaterials for hydrogen storage. **(a, b)** Non-auxetic and auxetic lattice metamaterial architectures. **(c)** Typical hexagonal honeycomb unit cell cell that constitutes a hexagonal lattice through tessellation. **(d)** Tri-member unit cell of the lattice metamaterial. Note that both the hexagonal and tri-member unit cells can be tesslated to form a hexagonal lattice. **(e)** 8-noded degenerated shell element for analyzing the cell walls of the lattice. **(f)** Geometry of curved a beam that is used as lattice cell walls. **(g)** Material property variation across the thickness for different power law indices. **(h)** Typical material distribution in a functionally graded beam across thickness. **(i)** Hydrogen storage tank with functionally graded metamaterial core. Note that multiple layers of 2D lattices (or a single lattice with the out-of-plane depth the same as the length of the tank) could be used along the cross-sectional plane of the tube. 3D lattices [76, 77] could also be incorporated adopting the concept of functionally graded cell walls. The lattice architectures could further be optimized based on application-specific mechanical loading conditions.

fuel will be reduced significantly as the honeycomb lattice can act as an active buffer. Most importantly, the proposed concept would lead to a breakthrough in developing load-bearing energy storage devices for automotive and aerospace applications. The proposed design can be aligned with the emerging futuristic concepts of fuel-filled structural components such as fuel-filled load bearing aircraft wings. The 2D or 3D lattice core architectures, as illustrated in Figure 1(i)(I, II), can further be optimized for an enhanced mechanical performance depending on the shape of the tank and application-specific loading conditions.

Functionally graded materials can exhibit remarkable tolerance towards extreme hot or cold environments and chemical surface degradation. Thus we propose to introduce functionally graded materials in the connecting beam-like elements of the lattice core as depicted in Figure 1(h). The outer sides of the proposed constituting beams are rich in ceramic (inert to hydrogen [78]) to shield the structure from extreme surrounding environmental effects, while the center part of the beam is rich in metal to enhance strength and stiffness.

Research on functionally graded metamaterials, specifically engineered to maximize nonlinear stiffness through the exploitation of elementary out-of-plane curvature, offers profound benefits for sustainability and environmental impact. Besides impacting the net-zero ambitions based on hydrogen fuel, these advanced engineered materials can revolutionize the aerospace industry by reducing the weight of structural components while offering adequate mechanical properties. Further the notion of load-bearing fuel storage components that can be integrated to the structural shapes of aerospace and automobile vehicles can lead to extremal fuel efficiency. This weight reduction directly translates into lower fuel consumption and emissions, significantly mitigating the carbon footprint of aerospace operations. The development of such sustainable materials not only aligns with environmental and economic goals, but also promotes responsible and efficient use of resources, paving the way for greener technologies.

3. Computational modeling of nonlinear functionally graded metamaterials

In this section, we provide the mathematical formulation for determining the effective elastic moduli of curved lattice metamaterials. For nonlinear finite element modeling of the functionally graded beam-like elements, accurate degenerated shell elements will be exploited, and subsequently the beam-level numerical results will be integrated with unit cell mechanics following a nonlinear semi-analytical framework to obtain the effective elastic properties of the lattices.

3.1. Curved functionally graded beams

A 3D degenerated shell element model has been used here to model the functionally graded beams. These elements are based on the three-dimensional continuum theory and exhibit similarities to 2-dimensional serendipity elements, with the additional capability of incorporating variations in the thickness direction. The creation of these elements is based on the degenerated solid approach, which uses Reissner-Mindlin assumptions to incorporate shear deformation and rotary inertia effects. As a result, the 3D field is simplified to a 2D field, described by mid-surface nodal variables.

3.1.1. Material properties of functionally graded beams

The material properties of functionally graded (FG) beams are assumed to vary along the thickness direction. In the present study, the outer sides of the beam are made up of ceramics and the inner side consists of metal (see Fig.1(h)). The power law distribution is adopted to calculate the equivalent material properties in the desired direction as:

$$\begin{aligned} E &= (E_c - E_m)\, V_c(z) + E_m \\ \rho &= (\rho_c - \rho_m)\, V_c(z) + \rho_m \\ \nu &= (\nu_c - \nu_m)\, V_c(z) + \nu_m \end{aligned} \tag{1}$$

where the subscript c and m represent ceramic and metallic constituents, respectively. The volume fraction of ceramic depends on the thickness coordinate and is expressed as:

$$V_c(z) = \left(\tfrac{2z+h}{2h}\right)^p \quad 0 \leqslant p \leqslant \infty \tag{2}$$

Here, p denotes the volume fraction index (also known as power law index). For $p = 0$, and $p{=}\infty$, the FG beam behaves like pure ceramic and metal, respectively.

3.1.2. Modelling of curved FG beams

In the beam model, an 8-noded degenerated shell element is employed with a natural coordinate system (ξ, η, ζ). This coordinate system is defined by the element's geometry rather than its orientation in the global coordinate system. The natural elements are scaled so that the sides of the parent elements are determined by $\xi = \pm 1, \eta = \pm 1$ and $\zeta = \pm 1$. The displacement field for a laminated FG beam is represented as follows:

$$\begin{Bmatrix} u \\ v \\ w \end{Bmatrix} = \sum N_i(\xi,\eta) \left[\begin{Bmatrix} u_i \\ v_i \\ w_i \end{Bmatrix} + \frac{\zeta t_i}{2} \begin{bmatrix} -v_{2i} & v_{1i} \end{bmatrix} \begin{Bmatrix} \alpha \\ \beta \end{Bmatrix} \right] \tag{3}$$

where N_i is the shape function of an 8 noded serendipity element, t_i is the thickness of the plate at node i, v_{1i} and v_{2i} are unit vectors along the x and y directions as

$$\begin{aligned} v_{1i} &= \begin{bmatrix} l_{1i} & m_{1i} & n_{1i} \end{bmatrix}^T \\ v_{2i} &= \begin{bmatrix} l_{2i} & m_{2i} & n_{2i} \end{bmatrix}^T \end{aligned} \tag{4}$$

α and β are rotation about x and y-axis respectively as shown in Fig. 1(e).

Since the elements might use a different coordinate system than the global coordinates, it is necessary to convert global strain components into local strain components. Considering geometric nonlinearity through Green's strain equation, the strain components in the local axis can be expressed as:

$$\varepsilon' = \varepsilon'_L + \varepsilon'_{NL} \tag{5}$$

Here, ε'_L and ε'_{NL} are the linear and nonlinear strain components, respectively. These components are calculated using following equations:

$$\varepsilon'_L = \begin{Bmatrix} \varepsilon'_{xL} \\ \varepsilon'_{yL} \\ \varepsilon'_{xyL} \\ \varepsilon'_{yzL} \\ \varepsilon'_{xzL} \end{Bmatrix} = \begin{Bmatrix} \frac{\partial u'}{\partial x'} \\ \frac{\partial v'}{\partial y'} \\ \frac{\partial u'}{\partial y'} + \frac{\partial v'}{\partial x'} \\ \frac{\partial v'}{\partial z'} + \frac{\partial w'}{\partial y'} \\ \frac{\partial u'}{\partial z'} + \frac{\partial w'}{\partial x'} \end{Bmatrix} = \underbrace{\begin{bmatrix} 1 & 0 & 0 & 0 & 0 & 0 & 0 & 0 & 0 \\ 0 & 0 & 0 & 0 & 1 & 0 & 0 & 0 & 0 \\ 0 & 1 & 0 & 1 & 0 & 0 & 0 & 0 & 0 \\ 0 & 0 & 0 & 0 & 0 & 1 & 0 & 1 & 0 \\ 0 & 0 & 1 & 0 & 0 & 0 & 1 & 0 & 0 \end{bmatrix}}_{[T_1]} \begin{Bmatrix} \frac{\partial u'}{\partial x'} \\ \frac{\partial u'}{\partial y'} \\ \frac{\partial u'}{\partial z'} \\ \frac{\partial v'}{\partial x'} \\ \frac{\partial v'}{\partial y'} \\ \frac{\partial v'}{\partial z'} \\ \frac{\partial w'}{\partial x'} \\ \frac{\partial w'}{\partial y'} \\ \frac{\partial w'}{\partial z'} \end{Bmatrix} \tag{6}$$

$$
\varepsilon'_{NL} = \begin{Bmatrix} \varepsilon'_{xNL} \\ \varepsilon'_{yNL} \\ \varepsilon'_{xyNL} \\ \varepsilon'_{yzNL} \\ \varepsilon'_{xzNL} \end{Bmatrix} = \begin{Bmatrix} \frac{1}{2}\left(\frac{\partial u'}{\partial x'}\right)^2 + \frac{1}{2}\left(\frac{\partial v'}{\partial x'}\right)^2 + \frac{1}{2}\left(\frac{\partial w'}{\partial x'}\right)^2 \\ \frac{1}{2}\left(\frac{\partial u'}{\partial y'}\right)^2 + \frac{1}{2}\left(\frac{\partial v'}{\partial y'}\right)^2 + \frac{1}{2}\left(\frac{\partial w'}{\partial y'}\right)^2 \\ \left(\frac{\partial u'}{\partial x'}\frac{\partial u'}{\partial y'}\right) + \left(\frac{\partial v'}{\partial x'}\frac{\partial v'}{\partial y'}\right) + \left(\frac{\partial w'}{\partial x'}\frac{\partial w'}{\partial y'}\right) \\ \left(\frac{\partial u'}{\partial y'}\frac{\partial u'}{\partial z'}\right) + \left(\frac{\partial v'}{\partial y'}\frac{\partial v'}{\partial z'}\right) + \left(\frac{\partial w'}{\partial y'}\frac{\partial w'}{\partial z'}\right) \\ \left(\frac{\partial u'}{\partial x'}\frac{\partial u'}{\partial z'}\right) + \left(\frac{\partial v'}{\partial x'}\frac{\partial v'}{\partial z'}\right) + \left(\frac{\partial w'}{\partial x'}\frac{\partial w'}{\partial z'}\right) \end{Bmatrix} =
$$

$$
\underbrace{\begin{bmatrix} \frac{1}{2}\frac{\partial u'}{\partial x'} & 0 & 0 & \frac{1}{2}\frac{\partial v'}{\partial x'} & 0 & 0 & \frac{1}{2}\frac{\partial w'}{\partial x'} & 0 & 0 \\ 0 & \frac{1}{2}\frac{\partial u'}{\partial y'} & 0 & 0 & \frac{1}{2}\frac{\partial v'}{\partial y'} & 0 & 0 & \frac{1}{2}\frac{\partial w'}{\partial y'} & 0 \\ 0 & \frac{\partial u'}{\partial x'} & 0 & 0 & \frac{\partial v'}{\partial x'} & 0 & 0 & \frac{\partial w'}{\partial x'} & 0 \\ 0 & 0 & \frac{\partial u'}{\partial y'} & 0 & 0 & \frac{\partial v'}{\partial y'} & 0 & 0 & \frac{\partial w'}{\partial y'} \\ 0 & 0 & \frac{\partial u'}{\partial x'} & 0 & 0 & \frac{\partial v'}{\partial x'} & 0 & 0 & \frac{\partial w'}{\partial x'} \end{bmatrix}}_{[T_2]} \begin{Bmatrix} \frac{\partial u'}{\partial x'} \\ \frac{\partial u'}{\partial y'} \\ \frac{\partial u'}{\partial z'} \\ \frac{\partial v'}{\partial x'} \\ \frac{\partial v'}{\partial y'} \\ \frac{\partial v'}{\partial z'} \\ \frac{\partial w'}{\partial x'} \\ \frac{\partial w'}{\partial y'} \\ \frac{\partial w'}{\partial z'} \end{Bmatrix} \tag{7}
$$

where $\frac{\partial u'}{\partial x'} = \frac{\partial u'}{\partial x}\frac{\partial x}{\partial x'} + \frac{\partial u'}{\partial y}\frac{\partial y}{\partial x'} + \frac{\partial u'}{\partial z}\frac{\partial z}{\partial x'}$ and $\frac{\partial u'}{\partial x} = \frac{\partial u}{\partial x}\frac{\partial u'}{\partial u} + \frac{\partial v}{\partial x}\frac{\partial u'}{\partial v} + \frac{\partial w}{\partial x}\frac{\partial u'}{\partial w}$. Here $\frac{\partial x}{\partial x'}, \frac{\partial y}{\partial x'}, \frac{\partial z}{\partial x'}, \frac{\partial x}{\partial y'}, \frac{\partial y}{\partial y'}, \ldots.$ and $\frac{\partial u'}{\partial u}, \frac{\partial u'}{\partial v}, \frac{\partial u'}{\partial w}, \frac{\partial v'}{\partial u}, \frac{\partial v'}{\partial v}, \ldots.$ are the direction cosines $(l_x, l_y, l_z, m_x, m_y ...)$ between global and local coordinate system which is calculated using the Jacobian matrix of the element.

$$
\begin{aligned}
(n_x, n_y, n_z) &= \left(\tfrac{dx}{d\xi}, \tfrac{dy}{d\xi}, \tfrac{dz}{d\xi}\right) \times \left(\tfrac{dx}{d\eta}, \tfrac{dy}{d\eta}, \tfrac{dz}{d\eta}\right) \\
(l_x, l_y, l_z) &= \tfrac{(n_x, n_y, n_z)}{|(n_x, n_y, n_z)|} \\
(m_x, m_y, m_z) &= (n_x, n_y, n_z) \times (l_x, l_y, l_z)
\end{aligned} \tag{8}
$$

Converting local strains to global strains, we get

$$\begin{Bmatrix} \frac{\partial u'}{\partial x'} \\ \frac{\partial u'}{\partial y'} \\ \frac{\partial u'}{\partial z'} \\ \frac{\partial v'}{\partial x'} \\ \frac{\partial v'}{\partial y'} \\ \frac{\partial v'}{\partial z'} \\ \frac{\partial w'}{\partial x'} \\ \frac{\partial w'}{\partial y'} \\ \frac{\partial w'}{\partial z'} \end{Bmatrix} = \underbrace{\begin{bmatrix} l_x l_x & l_x m_x & l_x n_x & m_x l_x & m_x m_x & m_x n_x & n_x l_x & n_x m_x & n_x n_x \\ l_x l_y & l_x m_y & l_x n_y & m_x l_y & m_x m_y & m_x n_y & n_x l_y & n_x m_y & n_x n_y \\ l_x l_z & l_x m_z & l_x n_z & m_x l_z & m_x m_z & m_x n_z & n_x l_z & n_x m_z & n_x n_z \\ l_y l_x & l_y m_x & l_y n_x & m_y l_x & m_y m_x & m_y n_x & n_y l_x & n_y m_x & n_y n_x \\ l_y l_y & l_y m_y & l_y n_y & m_y l_y & m_y m_y & m_y n_y & n_y l_y & n_y m_y & n_y n_y \\ l_y l_z & l_y m_z & l_y n_z & m_y l_z & m_y m_z & m_y n_z & n_y l_z & n_y m_z & n_y n_z \\ l_z l_x & l_z m_x & l_z n_x & m_z l_x & m_z m_x & m_z n_x & n_z l_x & n_z m_x & n_z n_x \\ l_z l_y & l_z m_y & l_z n_y & m_z l_y & m_z m_y & m_z n_y & n_z l_y & n_z m_y & n_z n_y \\ l_z l_z & l_z m_z & l_z n_z & m_z l_z & m_z m_z & m_z n_z & n_z l_z & n_z m_z & n_z n_z \end{bmatrix}}_{[T]} \begin{Bmatrix} \frac{\partial u}{\partial x} \\ \frac{\partial u}{\partial y} \\ \frac{\partial u}{\partial z} \\ \frac{\partial v}{\partial x} \\ \frac{\partial v}{\partial y} \\ \frac{\partial v}{\partial z} \\ \frac{\partial w}{\partial x} \\ \frac{\partial w}{\partial y} \\ \frac{\partial w}{\partial z} \end{Bmatrix} \tag{9}$$

The global strains can be written as

$$\begin{Bmatrix} \frac{\partial u}{\partial x} \\ \frac{\partial u}{\partial y} \\ \frac{\partial u}{\partial z} \\ \frac{\partial v}{\partial x} \\ \frac{\partial v}{\partial y} \\ \frac{\partial v}{\partial z} \\ \frac{\partial w}{\partial x} \\ \frac{\partial w}{\partial y} \\ \frac{\partial w}{\partial z} \end{Bmatrix} = \underbrace{\begin{bmatrix} \frac{\partial \xi}{\partial x} & \frac{\partial \eta}{\partial x} & \frac{\partial \zeta}{\partial x} & 0 & 0 & 0 & 0 & 0 & 0 \\ \frac{\partial \xi}{\partial y} & \frac{\partial \eta}{\partial y} & \frac{\partial \zeta}{\partial y} & 0 & 0 & 0 & 0 & 0 & 0 \\ \frac{\partial \xi}{\partial z} & \frac{\partial \eta}{\partial z} & \frac{\partial \zeta}{\partial z} & 0 & 0 & 0 & 0 & 0 & 0 \\ 0 & 0 & 0 & \frac{\partial \xi}{\partial x} & \frac{\partial \eta}{\partial x} & \frac{\partial \zeta}{\partial x} & 0 & 0 & 0 \\ 0 & 0 & 0 & \frac{\partial \xi}{\partial y} & \frac{\partial \eta}{\partial y} & \frac{\partial \zeta}{\partial y} & 0 & 0 & 0 \\ 0 & 0 & 0 & \frac{\partial \xi}{\partial z} & \frac{\partial \eta}{\partial z} & \frac{\partial \zeta}{\partial z} & 0 & 0 & 0 \\ 0 & 0 & 0 & 0 & 0 & 0 & \frac{\partial \xi}{\partial x} & \frac{\partial \eta}{\partial x} & \frac{\partial \zeta}{\partial x} \\ 0 & 0 & 0 & 0 & 0 & 0 & \frac{\partial \xi}{\partial y} & \frac{\partial \eta}{\partial y} & \frac{\partial \zeta}{\partial y} \\ 0 & 0 & 0 & 0 & 0 & 0 & \frac{\partial \xi}{\partial z} & \frac{\partial \eta}{\partial z} & \frac{\partial \zeta}{\partial z} \end{bmatrix}}_{[Jac]} \begin{Bmatrix} \frac{\partial u}{\partial \xi} \\ \frac{\partial u}{\partial \eta} \\ \frac{\partial u}{\partial \zeta} \\ \frac{\partial v}{\partial \xi} \\ \frac{\partial v}{\partial \eta} \\ \frac{\partial v}{\partial \zeta} \\ \frac{\partial w}{\partial \xi} \\ \frac{\partial w}{\partial \eta} \\ \frac{\partial w}{\partial \zeta} \end{Bmatrix} \tag{10}$$

where,

$$\begin{Bmatrix} \frac{\partial u}{\partial \xi} \\ \frac{\partial u}{\partial \eta} \\ \frac{\partial u}{\partial \zeta} \\ \frac{\partial v}{\partial \xi} \\ \frac{\partial v}{\partial \eta} \\ \frac{\partial v}{\partial \zeta} \\ \frac{\partial w}{\partial \xi} \\ \frac{\partial w}{\partial \eta} \\ \frac{\partial w}{\partial \zeta} \end{Bmatrix} = \sum_{i=1}^{8} \underbrace{\begin{bmatrix} \frac{\partial N_i}{\partial \xi} & 0 & 0 & -\frac{\partial N_i}{\partial \xi}\frac{\zeta t_i l_{2i}}{2} & \frac{\partial N_i}{\partial \xi}\frac{\zeta t_i l_{1i}}{2} \\ \frac{\partial N_i}{\partial \eta} & 0 & 0 & -\frac{\partial N_i}{\partial \eta}\frac{\zeta t_i l_{2i}}{2} & \frac{\partial N_i}{\partial \eta}\frac{\zeta t_i l_{1i}}{2} \\ 0 & 0 & 0 & -\frac{N_i t_i l_{2i}}{2} & \frac{N_i t_i l_{1i}}{2} \\ 0 & \frac{\partial N_i}{\partial \xi} & 0 & -\frac{\partial N_i}{\partial \xi}\frac{\zeta t_i m_{2i}}{2} & \frac{\partial N_i}{\partial \xi}\frac{\zeta t_i m_{1i}}{2} \\ 0 & \frac{\partial N_i}{\partial \eta} & 0 & -\frac{\partial N_i}{\partial \eta}\frac{\zeta t_i m_{2i}}{2} & \frac{\partial N_i}{\partial \eta}\frac{\zeta t_i m_{1i}}{2} \\ 0 & 0 & 0 & -\frac{N_i t_i m_{2i}}{2} & \frac{N_i t_i m_{1i}}{2} \\ 0 & 0 & \frac{\partial N_i}{\partial \xi} & -\frac{\partial N_i}{\partial \xi}\frac{\zeta t_i n_{2i}}{2} & \frac{\partial N_i}{\partial \xi}\frac{\zeta t_i n_{1i}}{2} \\ 0 & 0 & \frac{\partial N_i}{\partial \eta} & -\frac{\partial N_i}{\partial \eta}\frac{\zeta t_i n_{2i}}{2} & \frac{\partial N_i}{\partial \eta}\frac{\zeta t_i n_{1i}}{2} \\ 0 & 0 & 0 & -\frac{N_i t_i n_{2i}}{2} & \frac{N_i t_i n_{1i}}{2} \end{bmatrix}}_{[\partial N]} \begin{Bmatrix} u_i \\ v_i \\ w_i \\ \alpha_i \\ \beta_i \end{Bmatrix} \tag{11}$$

Strain-displacement matrix $[B]$ can be defined using equations (5, 6, 7, 9, 10, 11) as following:

$$[B] = [B_L] + [B_{NL}] = [T_1]\,[T]\,[Jac]\,[\partial N] + [T_2]\,[T]\,[Jac]\,[\partial N] \tag{12}$$

Stress-strain relationship matrix $[D]$ is taken as:

$$[D] = \frac{E}{(1-\upsilon^2)} \begin{bmatrix} 1 & \upsilon & 0 & 0 & 0 \\ \upsilon & 1 & 0 & 0 & 0 \\ 0 & 0 & \frac{(1-\upsilon)}{2} & 0 & 0 \\ 0 & 0 & 0 & \frac{K_s(1-\upsilon)}{2} & 0 \\ 0 & 0 & 0 & 0 & \frac{K_s(1-\upsilon)}{2} \end{bmatrix} \tag{13}$$

Here, E, ν, and K_s are effective modulus of elasticity, effective Poisson's ratio, and the shear correction factor for the functionally graded material. The stiffness matrix $[K]$ is expressed as:

$$[K] = \int\int\int [B]^T\,[D]\,[B]\,|J|\,d\xi d\eta d\zeta \tag{14}$$

After having the stiffness matrix, the conventional finite element operations can be followed to evaluate the deflection of the curved functionally graded beams under appropriate loading and boundary conditions to analyze the lattice further.

3.2. Effective nonlinear elastic properties of functionally graded lattices

The general formulation for determining the in-plane and out-of-plane effective material properties of a functionally graded lattice, taking into account both transverse and axial displacements, is presented here. Since we are considering geometrical nonlinearity of the beam while calculating the effective lattice-level material properties, the analysis will be carried out using incremental geometry updation until the deflection results converge. As the solution process is iterative, several geometric properties

of the unit cell will be updated in every iteration. Keeping this in mind, the presented state in the formulation from now on is depicted for i^{th} iteration.

3.2.1. E_1 of curved FG lattices

To determine the in-plane longitudinal modulus E_1 of the functionally graded lattice metamaterial, an in-plane far-field longitudinal stress (σ_1) is applied to the honeycomb. This stress induces both transverse and axial displacements (δ^i and δ_a^i) in the slant beams, as illustrated in Fig. 2(b). The slant beam is assumed to be fixed at one end and rotationally restrained at the other end. This boundary condition is essential for accurately calculating the axial and transverse displacements ensuring unit cell periodicity. The stress and strain can subsequently be determined using the following equations:

$$\sigma_1^i = \frac{P^i}{(h^i + l^i \sin\theta^i)\, W} \tag{15}$$

$$e_1^i = \frac{\delta^i \sin\theta^i + \delta_a^i \cos\theta^i}{l \cos\theta^i} \tag{16}$$

The expression of P^i is indicated in Fig. 2. The E_1 of the FG lattice metamaterial is determined using the following equation:

$$E_1 = \frac{\sigma_1^i}{e_1^i} \tag{17}$$

Here σ_1^i and e_1^i are the stress and strain, obtained at the final iteration when the results converge, respectively.

To calculate E_1 by considering only transverse deflection, one can disregard the axial deflection and use the above equations without any modifications. The difference between the E_1 values obtained from considering only transverse displacement versus both transverse and axial displacements is minimal, as the axial displacement is significantly smaller than the transverse displacement. However, the relative influence of the axial deformation component will depend on the cell angle.

3.2.2. E_2 of curved FG lattices

To determine the in-plane transverse Young's modulus E_2 of the lattice, in-plane far-field transverse stresses are applied to the lattice, and the total in-plane transverse displacement is measured. This process involves calculating the transverse and axial displacements (δ^i and δ_a^{li}) of the functionally graded slanted beam and the axial displacement (δ_a^{hi}) of the vertical beam within the honeycomb cell, as depicted in Fig. 2(d).

To obtain the total transverse displacement of the lattice cell under in-plane transverse stress, the slanted beam is subjected to an inclined load ($P^i/2$), and its deflections are assessed. As illustrated in Fig. 2(b), the slanted beam is assumed to be fixed at one end and rotationally restrained at the other

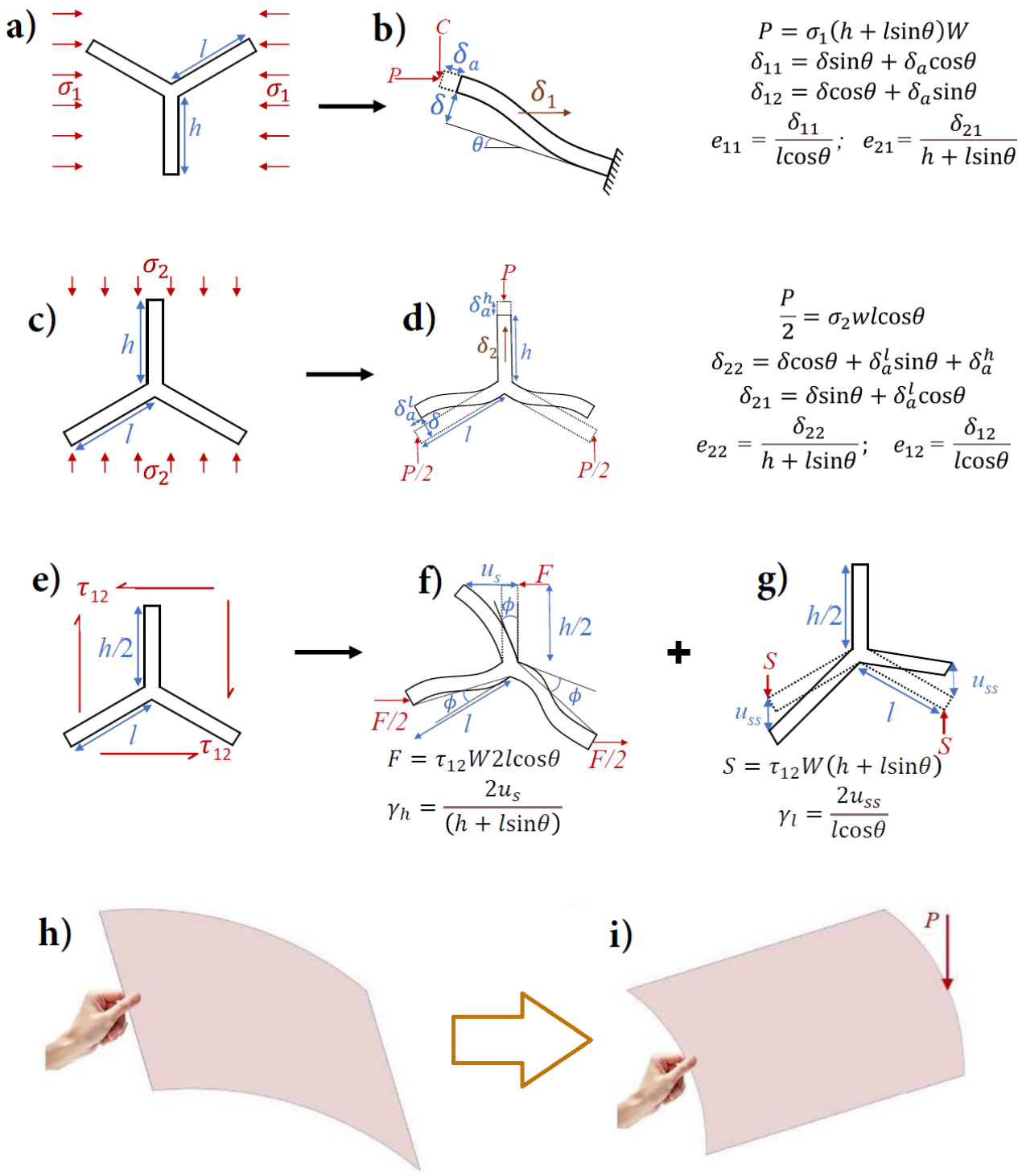

Figure 2: Unit cell based mechanics of transversely curved functionally graded lattices. **(a)** In-plane longitudinal compressive loading on the lattice cell to determine effective E_1 of the lattice. **(b)** Deformed slanted beam for calculating E_1, considering both transverse and axial deflection. **(c)** In-plane transverse compressive loading on the lattice cell to determine effective E_2 of the lattice. **(d)** Deformed lattice cell for calculating E_2, considering both transverse and axial deflection. **(e)** In-plane shear loading on the lattice cell to determine effective G_{12} of the lattice. **(f)** Deformed lattice cell under the horizontal component of τ_{12} for calculating G_{12} of the lattice. **(g)** Deformed lattice cell under the vertical component of τ_{12} for calculating G_{12} of the lattice. **(h, i)** Demonstration of transverse curvature induced enhancement in bending stiffness considering a typical experiment with a sheet of paper. We exploit such physical understanding to increase the in-plane stiffness of hexagonal lattices where the beam-like constituting elements are architected in the out-of-plane direction with transverse curvature.

end for ensuring unit cell periodicity. For calculating the axial displacement in the vertical beam of the honeycomb cell, a separate analysis is conducted by applying an axial load (P^i) to the vertical beam, which is assumed to be fixed at one end and free at the other end for the axial deflection calculation. The stress and strain in the lattice along in-plane transverse direction are then computed using the following equations:

$$\sigma_2^i = \frac{P^i}{W\left(l^i \cos\theta^i\right)} \tag{18}$$

$$e_2^i = \frac{\delta^i \cos\theta^i + \delta_a^{li} \sin\theta^i + \delta_a^{hi}}{h^i + l^i \sin\theta^i} \tag{19}$$

The expression of P^i is indicated in Fig. 2. The effective Young's modulus E_2 of FG lattice metamaterial is calculated using equation:

$$E_2 = \frac{\sigma_2^i}{e_2^i} \tag{20}$$

Here σ_2^i and e_2^i are the stress and strain values, obtained at the final iteration when the results converge, respectively.

To calculate E_2 by considering only transverse deflection, one can disregard the axial deflection of the slanted and vertical beams, and use the above equations as they are. The difference between the E_2 values obtained from considering only transverse displacement versus both transverse and axial displacements is minimal, since the axial displacement is significantly smaller than the transverse displacement. However, the relative influence of the axial deformation component will depend on the cell angle.

3.2.3. E_3 of curved FG lattices

To determine the out-of-plane transverse Young's modulus E_3 of the FG lattice metamaterial, an out-of-plane transverse stress is applied to the Y-shaped unit cell. In this case, a uniform pressure p^i is exerted on the top face of the cell, while the bottom face is assumed to be fixed (refer to Fig. 3(a, b)). The deflection (δ_z^i) resulting from the applied pressure is calculated to assess the response of the lattice cell. This deflection is then used to find the stress and strain using the following equations:

$$\sigma_3^i = \frac{p^i\left(h^i + 2l^i\right)t}{\left(h^i + l^i \sin\theta^i\right)\left(2l^i \cos\theta^i\right)} \tag{21}$$

$$e_3^i = \frac{\delta_z^i}{W} \tag{22}$$

The expression of p is indicated in Fig. 3. E_3 of FG lattice metamaterial is calculated using equation:

$$E_3 = \frac{\sigma_3^i}{e_3^i} \tag{23}$$

Here σ_3^i and e_3^i are the stress and strain values, obtained at the final iteration when the results converge, respectively. It may be noted that the value of E_3 reduces in lattices with transversely curved cell walls

compared to conventional straight cell walls due to the involvement of bending component. This results in a reduction in disparity between the in-plane and out-of-plane Young's moduli in hexagonal lattices where the in-plane mechanics is dominated by bending deformation of the cell walls.

Note that the out-of-plane specific elastic moduli of straight-wall hexagonal metamaterials are orders of magnitude higher than their in-plane elastic moduli, thus making them weak in in-plane loading conditions. The proposed curved cell wall metamaterials can lead to a large gain in in-plane effective moduli by marginal compromise in the out-of-plane moduli. Such designs make the metamaterial suitable for applications under multi-modal loading conditions.

3.2.4. G_{12} of curved FG lattices

To calculate the in-plane shear modulus G_{12} of the lattice metamaterial, an in-plane far-field shear stress τ_{12}^i is applied to the lattice, resulting in two force components, F^i and S^i. The effects of these force components need to be evaluated separately, as illustrated in Fig. 2(f) and 2(g). Note that we consider half length of the vertical cell wall to exploit the fact that bending moment at the middle of the cell wall becomes zero under both-end rotationally restrained boundary condition (this is enforced to maintain unit cell level periodicity) and the half beam can effectively be treated as a cantilever beam.

First, we consider the effect of the horizontal coupled force components of the in-plane shear stress, as shown in Fig. 2(f). In this case, the junction undergoes a rotation of angle ϕ in addition to the transverse deflection of the vertical member of the lattice cell. To determine the rotational angle ϕ^i, a force of magnitude $(F^i/2)$ is applied to the slanted beam of the lattice cell, which is fixed at one end and rotationally restrained at the other (not that such boundary conditions ensure periodicity of the unit cells). The rotation angle ϕ^i is calculated based on dividing the transverse deflection of the slanted beam by the length of the slanted beam.

The horizontal displacement of the lattice cell, denoted as u_s^i, is the sum of the displacement of the vertical beam due to the horizontal force (F^i) and the displacement resulting from the rotation of the vertical beam. The horizontal displacement u_s^i can be calculated using the following equation:

$$u_s^i = \frac{1}{2}\phi^i h^i + \delta^{hi} \tag{24}$$

where δ^{hi} represents the transverse displacement of the vertical beam due to the horizontal force F^i. The strain resulting from the horizontal component of the in-plane shear stress τ_{12}^i is determined using the following equation:

$$\gamma_h^i = \frac{2u_s^i}{(h^i + l^i \sin\theta^i)} \tag{25}$$

Now the strain due to vertical coupled force components of the in-plane shear stress τ_{12}^i needs to be

calculated. Due to the vertical coupled forces, the slanted beams of lattice cell will experience vertical deflection u^i_{ss}. The deflection can be calculated using equation:

$$u_{ss} = \frac{\delta^i}{\cos\theta^i} \tag{26}$$

Here, δ^i is the transverse deflection of slanted beam due to inclined load S. The strain due to vertical component of the in-plane shear stress τ_{12} is determined from the equation:

$$\gamma^i_l = \frac{2u^i_{ss}}{l\cos\theta^i} \tag{27}$$

It is worth noting that the slant members will not experience any bending under the application of S and rotationally restrained ends of the slant beams, while the deformation will solely be due to axial effects as indicated in Fig. 2(g).

The total shear strain is calculated using equation:

$$\gamma^i_{12} = \gamma^i_l + \gamma^i_h \tag{28}$$

The equation for calculating in-plane shear modulus (G_{12}) is given as:

$$G_{12} = \frac{\tau^i_{12}}{\gamma^i_{12}} \tag{29}$$

Here τ^i_{12} and γ^i_{12} are the effective stress and strain, obtained at the final iteration when the results converge, respectively.

It can be noted that the above formulation accounts for both bending and axial deflections of the beams. To calculate G_{12} by considering only transverse deflection, one can disregard the axial deflection of the slanted and vertical beams, and use the above equations as they are.

3.2.5. G_{23} of curved FG lattice

To calculate the out-of-plane shear moduli G_{23} and G_{13}, we need the effective in-plane shear modulus $\bar{G_{12}}$ of the curved beam. This effective $\bar{G_{12}}$ will differ from the intrinsic shear modulus of the FG material due to the beam's curvature. Note that $\bar{G_{12}}$ has no relation with the in-plane effective shear modulus of the lattice, G_{12}. To determine the effective in-plane shear modulus $\bar{G_{12}}$ of the curved beam, a curved shell-like structure with its bottom side fixed, as shown in Fig. 3(e), is considered. A point load P^i is applied on the top of the beam, parallel to the fixed side. The effective shear modulus of the curved beam is then calculated using the following equation:

$$\bar{G_{12}} = \frac{P^i W}{\delta^i_s l^i t} \tag{30}$$

Here, P^i, W, δ^i_s, l^i, and t are applied load, width of beam, shear deflection, length of beam, and thickness of beam as shown in Fig. 3(e).

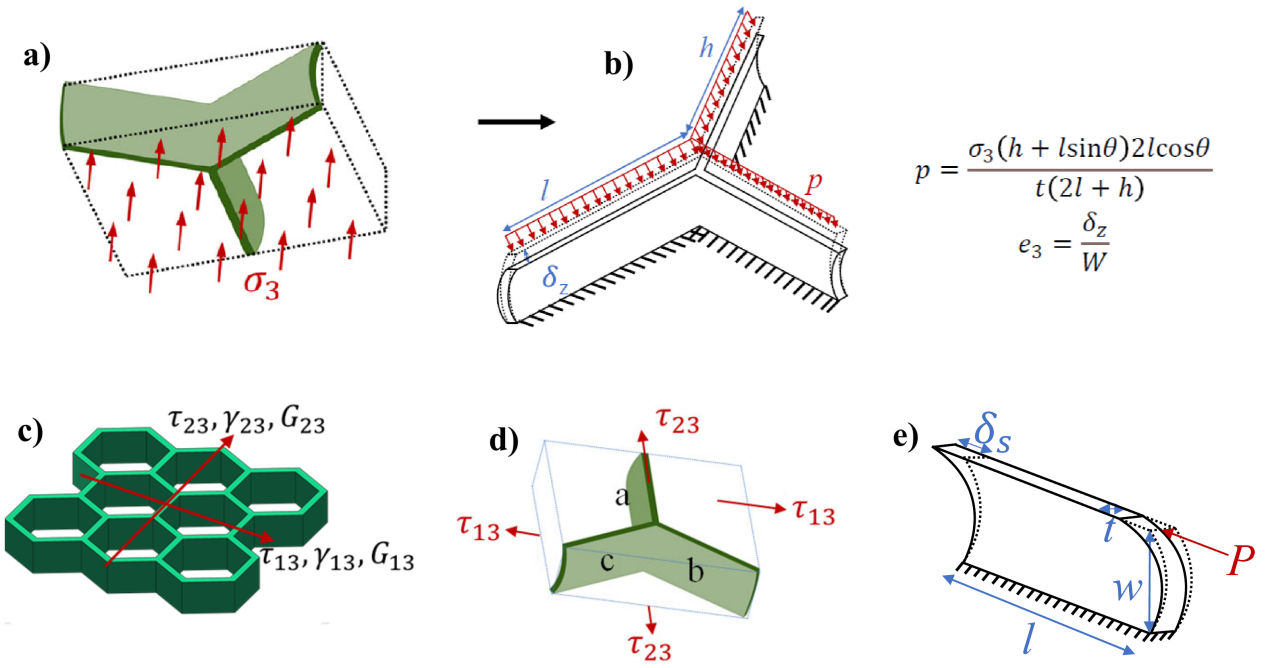

Figure 3: Out-of-plane unit cell mechanics of hexagonal lattices. **(a)** Out-of-plane compressive loading on the lattice cell to determine effective E_3. **(b)** Deformed lattice cell under σ_3 for calculating E_3 of the lattice. **(c)** Out-of-plane shear stresses at the lattice level. **(d)** Out-of-plane shear stresses at the unit cell level. **(e)** Calculation of effective shear modulus of curved beams. Note that the direction of curvature in the cell walls does not influence the effective elastic properties under the imposed rotationally-restrained boundary condition. Thus, the beams may have curvature in any direction without affecting the relative joint deformations and the effective elastic moduli.

The out-of-plane shear moduli of the lattice are challenging to calculate due to the non-uniform deformation of each cell walls. However, the upper and lower limits of the shear moduli can be determined using the minimum potential energy and minimum complementary energy theorems, respectively. To find G_{23} of the lattice, the lattice is subjected to an out-of-plane stress τ_{23}, as illustrated in Fig. 3(c, d) (the stresses τ_{23} and the corresponding strain γ_{23} should be considered). The cell beams a, b, and c will experience shear strains due to the shear stress τ_{23}. These strains can be expressed in terms of the cell strain γ_{23} as follows:

$$\begin{aligned} \gamma_a &= \gamma_{23} \\ \gamma_b &= \gamma_{23} \sin\theta \\ \gamma_c &= \gamma_{23} \sin\theta \end{aligned} \tag{31}$$

The minimum potential energy theorem can be expressed as an inequality form

$$\frac{1}{2} G_{23} \gamma_{23}^2 V \leq \frac{1}{2} \sum_i \left(\bar{G_{12}} \gamma_i^2 V_i \right) \tag{32}$$

Here, V is the volume of lattice cell, $\bar{G_{12}}$ is the effective shear modulus of curved beam (as discussed in the preceding paragraph), γ_i is the strain of beam i, and V_i is the volume of beam i. The volume of

lattice cell can be calculated as:

$$V = 2Wl\cos\theta\,(h + 2l\sin\theta) \tag{33}$$

The volume of cured beam of length l, width W, radius of curvature R, and thickness t can be calculated from equation:

$$V_b = 2R\sin^{-1}\left(\frac{W}{2R}\right)lt \tag{34}$$

Substituting Eq. 33 and 34 in Eq. 32 results in equation:

$$G_{23} \leq \frac{1}{2}\bar{G_{12}}\left(\frac{\frac{h}{l} + 2\sin^2\theta}{\left(\frac{h}{l} + \sin\theta\right)\cos\theta}\right)\left(\frac{2R\sin^{-1}\left(\frac{W}{2R}\right)t}{Wl}\right) \tag{35}$$

The upper limit of G_{23} can be determined from minimum complementary energy equation which is given as:

$$\frac{1}{2}\frac{\tau_{23}^2}{G_{23}}V \leq \frac{1}{2}\sum_i\left(\frac{\tau_i^2}{\bar{G_{12}}}V_i\right) \tag{36}$$

where, τ_{23} is the shear stress at the cell level and τ_i is the shear stress at beam i. The shear stress at beams b and c will be same due to symmetry. Also taking taking equilibrium at node in the direction X_3 will result in:

$$\tau_a = \tau_b + \tau_c = 2\tau_b \tag{37}$$

The shear stresses at the beam level can be related to the shear stress at the cell level by equating total shear force acting on the cell with the total shear force acting on the beam. The equilibrium equation will be:

$$2\tau_{23}l\,(h + l\sin\theta)\cos\theta = 2\tau_b tl\sin\theta + \tau_a th \tag{38}$$

or

$$\tau_b = \tau_{23}\cos\theta\frac{l}{t} \tag{39}$$

Combining Eqs. 36, 39, and 33 gives:

$$G_{23} \geq \bar{G_{12}}\left(\frac{\frac{h}{l} + \sin\theta}{\left(\frac{2h}{l} + 1\right)\cos\theta}\right)\left(\frac{2R\sin^{-1}\left(\frac{W}{2R}\right)t}{Wl}\right) \tag{40}$$

It should be noted that Eq. 40 and Eq. 35 are not same hence the upper and lower limit of G_{23} will be different in general. The upper and lower limit of G_{23} may coincide for some special cases such as for $l = h$. In the result section, the lower limit of G_{23} is presented.

As a special case, it is interesting to note that Eq. 35 and 40 reduce to G_{23} for lattice with straight beams presented by Gibson and Ashby [31] as R approaches infinity, i.e.

$$\lim_{R\to\infty} 2R\sin^{-1}\left(\frac{W}{2R}\right) = W \tag{41}$$

that will transform Eq. 35 and 40 into

$$G_{23} \leq \frac{1}{2}\bar{G_{12}} \left(\frac{\frac{h}{l} + 2\sin^2\theta}{\left(\frac{h}{l} + \sin\theta\right)\cos\theta} \right) \left(\frac{t}{l}\right) \tag{42}$$

$$G_{23} \geq \bar{G_{12}} \left(\frac{\frac{h}{l} + \sin\theta}{\left(\frac{2h}{l} + 1\right)\cos\theta} \right) \left(\frac{t}{l}\right) \tag{43}$$

The above discussion present an exact analytical validation of the limits of G_{23}.

3.2.6. G_{13} of curved FG lattice

The equations for out of plane shear modulus G_{13} will be derived in the same manner as it is done for G_{23} (refer to Fig. 3(c, d), where the stresses τ_{13} and the corresponding strain γ_{13} should be considered). The Lower limit of G_{13} will be derived from minimum potential energy theorem:

$$\frac{1}{2}G_{13}\gamma_{13}^2 V \leq \frac{1}{2}\sum_i \left(\bar{G_{12}}\gamma_i^2 V_i\right) \tag{44}$$

Here, V is the volume of lattice cell, $\bar{G_{12}}$ is the effective shear modulus of curved beam, and γ_i is the strain of beam i which can be represented in terms of cell strain γ_{13} as follows:

$$\begin{aligned} \gamma_a &= 0 \\ \gamma_b &= \gamma_{13}\cos\theta \\ \gamma_c &= \gamma_{13}\cos\theta \end{aligned} \tag{45}$$

Substituting 45 and 33 into 44, we get:

$$G_{13} \leq \bar{G_{12}} \left(\frac{\cos\theta}{\frac{h}{l} + \sin\theta} \right) \left(\frac{2R\sin^{-1}\left(\frac{W}{2R}\right) t}{Wl} \right) \tag{46}$$

The upper limit of G_{13} can be determined from minimum complementary energy equation which is given as:

$$\frac{1}{2}\frac{\tau_{13}^2}{G_{13}} V \leq \frac{1}{2}\sum_i \left(\frac{\tau_i^2}{\bar{G_{12}}} V_i \right) \tag{47}$$

where, τ_{13} is the shear stress at the cell level and τ_i is the shear stress at beam i. The shear stress at beam a will be zero as shear force is applied perpendicular to beam a, resulting in pure bending of beam a. The shear stress at beams b and c will be same due to symmetry and can be related to the shear stress at the cell level by equating total shear force acting on the cell with the total shear force acting on the beam. The equilibrium equation will be:

$$2\tau_{13} l \left(h + l\sin\theta\right)\cos\theta = 2\tau_b t l \cos\theta \tag{48}$$

Combining Eqs. 47, 48, and 47 gives:

$$G_{13} \leq \bar{G_{12}} \left(\frac{\cos\theta}{\frac{h}{l} + \sin\theta} \right) \left(\frac{2R\sin^{-1}\left(\frac{W}{2R}\right) t}{Wl} \right) \tag{49}$$

We observe that Eq. 46 and Eq. 49 are identical and thus give exact result of G_{13} as

$$G_{13} = \bar{G_{12}} \left(\frac{\cos\theta}{\frac{h}{l} + \sin\theta} \right) \left(\frac{2R\sin^{-1}\left(\frac{W}{2R}\right) t}{Wl} \right) \tag{50}$$

Eq. 50 can be used for straight beams by using very high value of R. As R approaches infinity, as a special case of conventional straight cell walls, based on Eq. 41, the Eq. 50 reduces to

$$G_{13} \leq \bar{G_{12}} \left(\frac{\cos\theta}{\frac{h}{l} + \sin\theta} \right) \left(\frac{t}{l} \right) \tag{51}$$

The above equation exactly matches with the formulation of Gibson and Ashby [31], and thus, provides an exact analytical validation for G_{13}.

3.2.7. Poisson's ratios of curved FG lattices

The in-plane Poisson's ratio ν_{12} is calculated using equation:

$$\nu_{12} = \frac{-e_{21}}{e_{11}} \tag{52}$$

where e_{11} and e_{21} are longitudinal strain and transverse strain respectively due to load applied in longitudinal direction.

The in-plane Poisson ratio ν_{21} is calculated using equation:

$$\nu_{21} = \frac{-e_{12}}{e_{22}} \tag{53}$$

where e_{22} and e_{12} are transverse strain and longitudinal strain respectively due to load applied in the transverse direction. Note that the strain components e_{11}, e_{21}, e_{22} and e_{12} can be evaluated from the respective deformation components, as depicted in Fig. 2(a-d).

It should also be noted that the out of plane Poisson's ratios ν_{23} and ν_{13} are negligible and can be considered zero (similar to conventional straight cell walls). However, ν_{32} and ν_{31} for the current curved beam-like cell walls would be slightly less than the Poisson's ratio of intrinsic materials, depending on the degree of curvature. Specifically, the factor of reduction f_r can be quantified as $f_r = \frac{e_{cz}}{e_{sz}}$, where e_{cz} and e_{sz} are the strain in direction 3 under an applied far-field stress in the same direction for a curved cell wall and straight cell wall respectively. Note that ν_{32} and ν_{31} become equal to the Poisson's ratio of intrinsic materials in case of conventional straight beam-like cell walls.

3.2.8. Density of curved FG lattice

The density of lattice metamaterials is calculated using the density of functionally graded material and the volume of unit cell of the metamaterial. The equation for finding the density of lattice metamaterial is given as:

$$\rho = \frac{M}{V} \tag{54}$$

where, M is the mass of lattice cell and V is the volume of lattice cell calculated from Eq. 33. The mass of lattice cell can be calculated from equation:

$$M = \rho_s \left(2l + h\right) A \tag{55}$$

Here, ρ_s is the density of functionally graded material and A is the area of cross section of curved beam. This area will increase with decrease in the radius of curvature. Using Eq. 33, 55, and 54, we get:

$$\rho = \frac{A \left(h + 2l\right) \rho_s}{W \left(h + l \sin\theta\right) 2l \cos\theta} \tag{56}$$

4. Results and discussion

This section presents numerical results for characterizing the effective nonlinear elastic moduli of curved functionally graded lattice metamaterials. We have investigated the impact of beam-level curvature variation along with unit cell geometric parameters and gradation properties. First we will validate the computational model with existing literature considering beam-level deformation (accounting for (a) isotropic and functionally graded beams, (b) curved and straight cross-sectional geometries, and (c) linear and nonlinear deformation) and unit cell level homogenized properties (linear and nonlinear), and subsequently, new results will be presented. We have preferred to use results available in the open literature here as they provide confidence from third-party cross-validation.

4.1. Convergence study and validation

A convergence study is conducted to determine suitable element size for the subsequent numerical investigation. In this study, an isotropic curved cantilever beam with dimensions of 50 mm length, 10 mm width, and 2 mm thickness is considered. The material properties of the beam are specified as Young's modulus (E) of 200 GPa and Poisson's ratio (ν) of 0.3. The beam is subjected to a point load of 1000 N at the free end. The results presented in Table 1 demonstrate that a mesh size of 15 $\times$ 5 achieves convergence for all investigated curvatures. To ensure accuracy and consistency across our simulations, we will adopt this element size (15 $\times$ 5) for all subsequent analyses.

For validation of straight isotropic beams, we have considered beams with dimensions of 400 mm $\times$ 25 mm $\times$ 0.4 mm, referencing the work of Belendez et al. [79]. These beams are assigned isotropic

Table 1: Maximum transverse displacement (mm) of a cantilever beam considering different mesh sizes for convergence study.

R_x/W	8×3	8×4	8×5	10×4	10×5	10×6	12×5	12×6	15×5	15×6
0.51	0.479	0.527	0.576	0.640	0.681	0.702	0.763	0.7665	0.782	0.782
1	3.255	3.426	3.569	3.837	3.976	4.058	4.227	4.2266	4.269	4.269
2	69.77	71.20	72.28	74.13	76.43	77.59	79.18	79.18	79.18	79.18

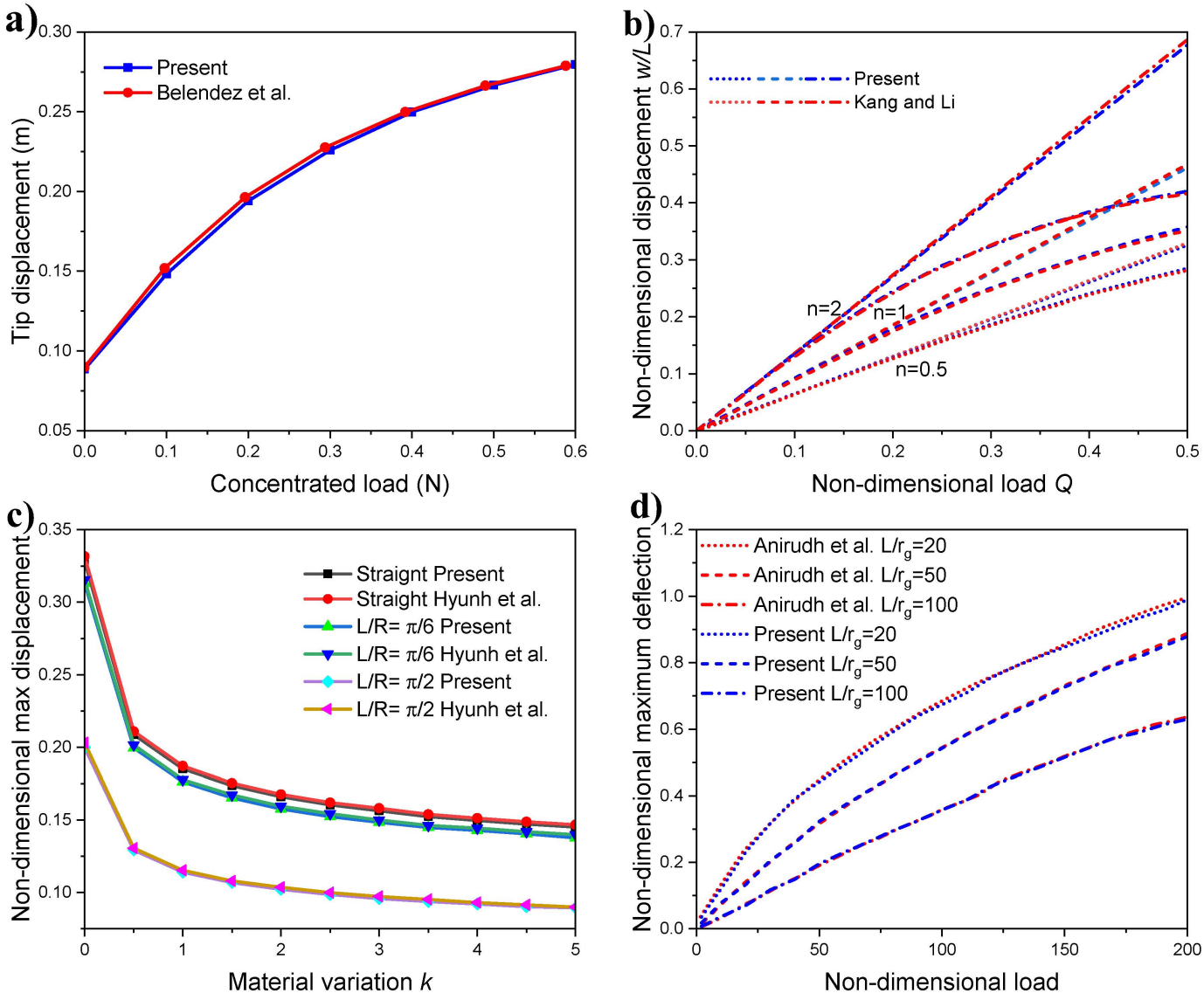

Figure 4: Validation of isotropic and functionally graded beams for both curved and straight crosssections under varying loads. (a) Straight isotropic cantilever beams with multiple loads (validated with Belendez et al. [79]) **(b)** Straight functionally graded cantilever beams for both linear and nonlinear results (validated with Kang and Li. [80]) **(c)** Curved funtionally graded linear cantilever beams with various curvatures (validated with Hyunh et al. [81]) **(d)** Nonlinear curved functionally graded cantilever beams with various curvatures (validated with Anirudh et al. [82]).

material properties of Young's modulus (E) = 200 GPa and Poisson's ratio (ν) = 0.3. One end of the beam is fixed, while the other end is free and subjected to a perpendicular point load. To account for geometrical nonlinearity, multiple load cases are simulated to record displacements. The resulting data

exhibit close agreement with the experimental findings of Belendez et al. [79], as shown in Fig. 4(a).

Both the linear and nonlinear models of functionally graded straight beams have been rigorously validated using results from Kang and Li [80]. Kang and Li presented non-dimensionalized displacement data across various non-dimensional loading conditions for multiple volume fractions. Our formulation has been found to be in excellent agreement with their results, as illustrated in Fig 4(b).

Furthermore, we have undertaken the validation of linear model for functionally graded curved beams, corroborating our findings with those of Hyunh et al. [81]. Hyunh et al. presented non-dimensionalized maximum displacement data for multiple volume fractions and various curvature values. Our formulation consistently exhibits strong agreement with their findings, as indicated in Fig 4(c).

Finally, the nonlinear model for functionally graded curved beams has been validated using data from Anirudh et al. [82]. Anirudh et al. provided non-dimensionalized maximum displacement data under multiple non-dimensional loading conditions for various curvature values. Our formulation demonstrates robust alignment with their results, as depicted in Fig 4(d).

To validate the computational model at the lattice level, we have focused on linear isotropic straight beams as this is sufficient to establish the accuracy of unit cell mechanics based on an accurate beam deformation model. The material properties used in this study are those of an isotropic material, with Young's modulus (E) = 210 GPa and Poisson's ratio (ν) = 0.3. The honeycomb cell's slanted beams have the following dimensions: length (l) of 20 mm, width of 2 mm, and thickness of 0.5 mm . The study encompasses an array of cell angles, ranging from -45° to 45°, and considers two distinct h/l ratios. To assess the accuracy and reliability of the current computational model, we have compared our results against both Gibson and Ashby's formulation [31] and those of Tiwari et al. [50]. The comparison reveals a high degree of agreement among all sets of results, as shown in Figs. 5 and 6. It's important to note that for an h/l ratio of 1, we only presented results for cell angles ranging from -30° to 45° since it is physically impossible to construct an auxetic lattice with a cell angle of -45° for an h/l ratio of 1.

The validation process extended beyond the linear lattice level. To validate the nonlinear lattice model, we have compared our results with those obtained by Ghuku and Mukhopadhyay [49]. The nonlinear validation considers a vertical beam with a length (h) of 3.67 mm, thickness of 0.01835 mm, and h/l ratio of 2. We have compared the non-dimensional in-plane Young's modulus calculated under various stresses with their findings. The obtained results are in good agreement with those of Ghuku and Mukhopadhyay [49] as shown in Fig. 7.

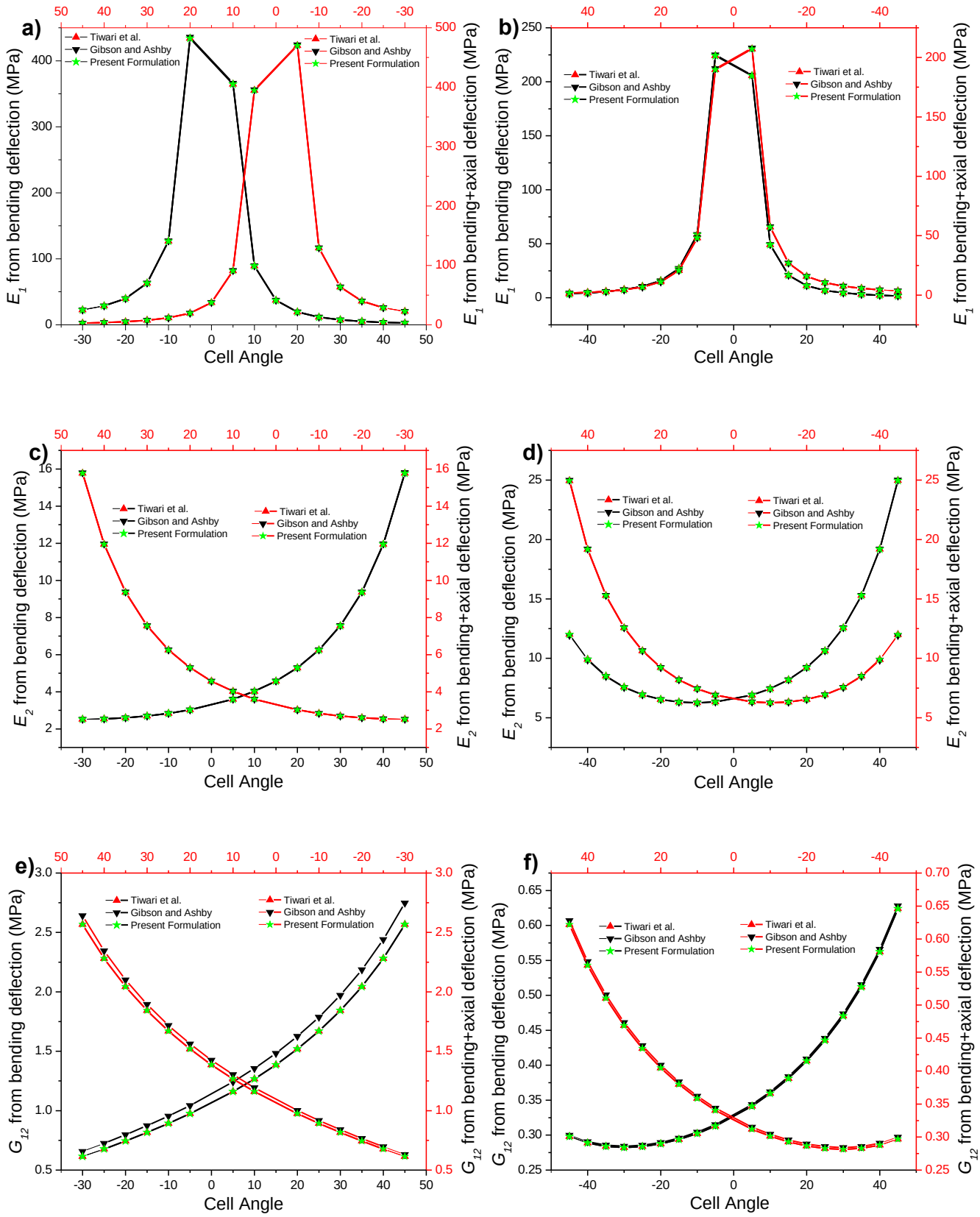

Figure 5: Validation considering in-plane effective material properties of straight isotropic lattice metamaterials. **(a)** Effective E_1 of straight isotropic lattice metamaterials considering h/l ratio as 1 and different cell angles **(b)** Effective E_1 of straight isotropic lattice metamaterials considering h/l ratio as 2 and different cell angles **(c)** Effective E_2 of straight isotropic lattice metamaterials considering h/l ratio as 1 and different cell angles **(d)** Effective E_2 of straight isotropic lattice metamaterials considering h/l ratio as 2 and different cell angles **(e)** Effective G_{12} of straight isotropic lattice metamaterials considering h/l ratio as 1 and different cell angles **(f)** Effective G_{12} of straight isotropic lattice metamaterials considering h/l ratio as 2 and different cell angles.

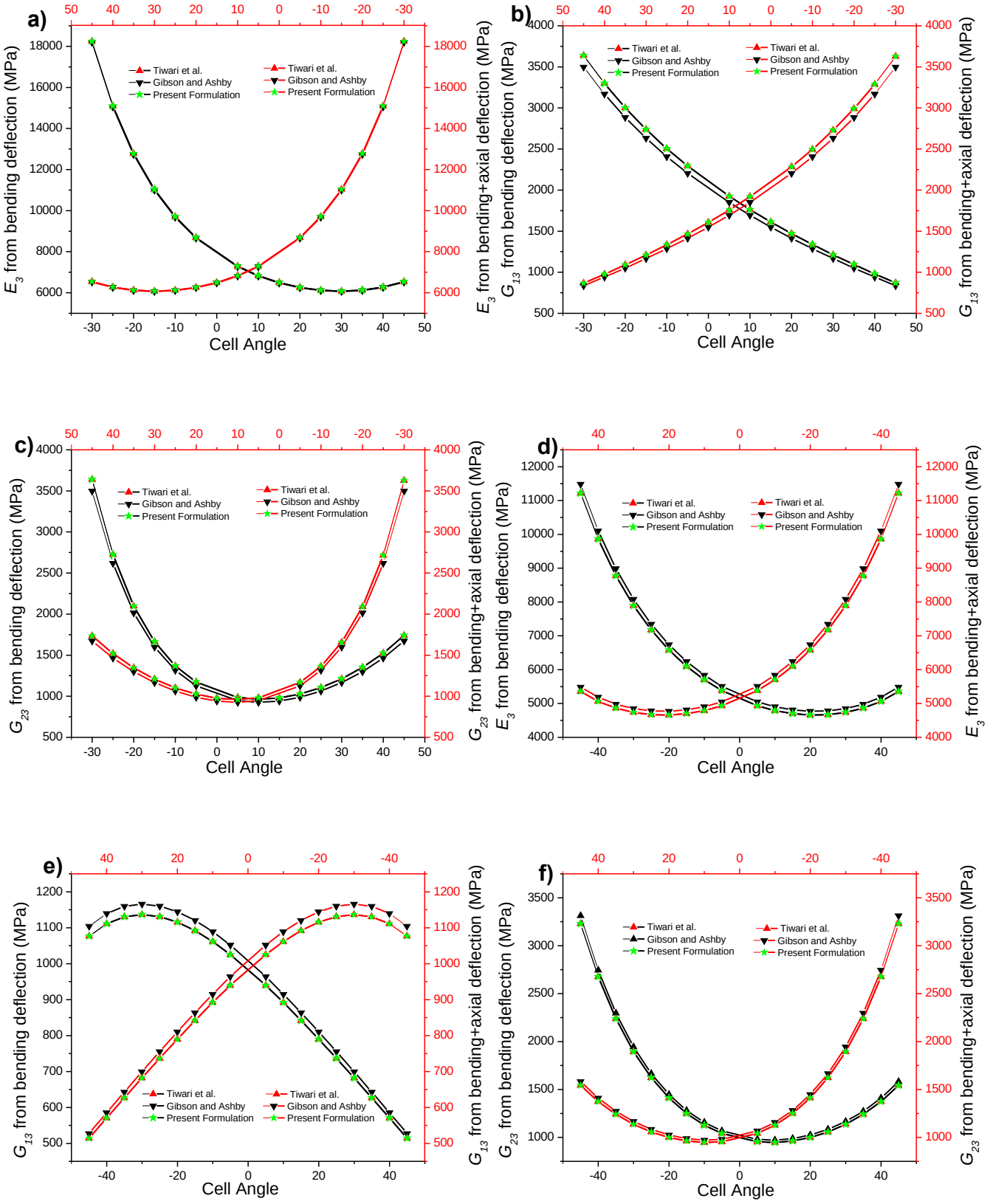

Figure 6: Validation of effective out-of-plane material properties considering straight isotropic lattice metamaterials. **(a)** Effective E_3 of straight isotropic lattice metamaterials considering h/l ratio as 1 and different cell angles **(b)** Effective E_3 of straight isotropic lattice metamaterials considering h/l ratio as 2 and different cell angles **(c)** Effective G_{23} of straight isotropic lattice metamaterials considering h/l ratio as 1 and different cell angles **(d)** Effective G_{23} of straight isotropic lattice metamaterials considering h/l ratio as 2 and different cell angles **(e)** Effective G_{13} of straight isotropic lattice metamaterials considering h/l ratio as 1 and different cell angles **(f)** Effective G_{13} of straight isotropic lattice metamaterials considering h/l ratio as 2 and different cell angles.

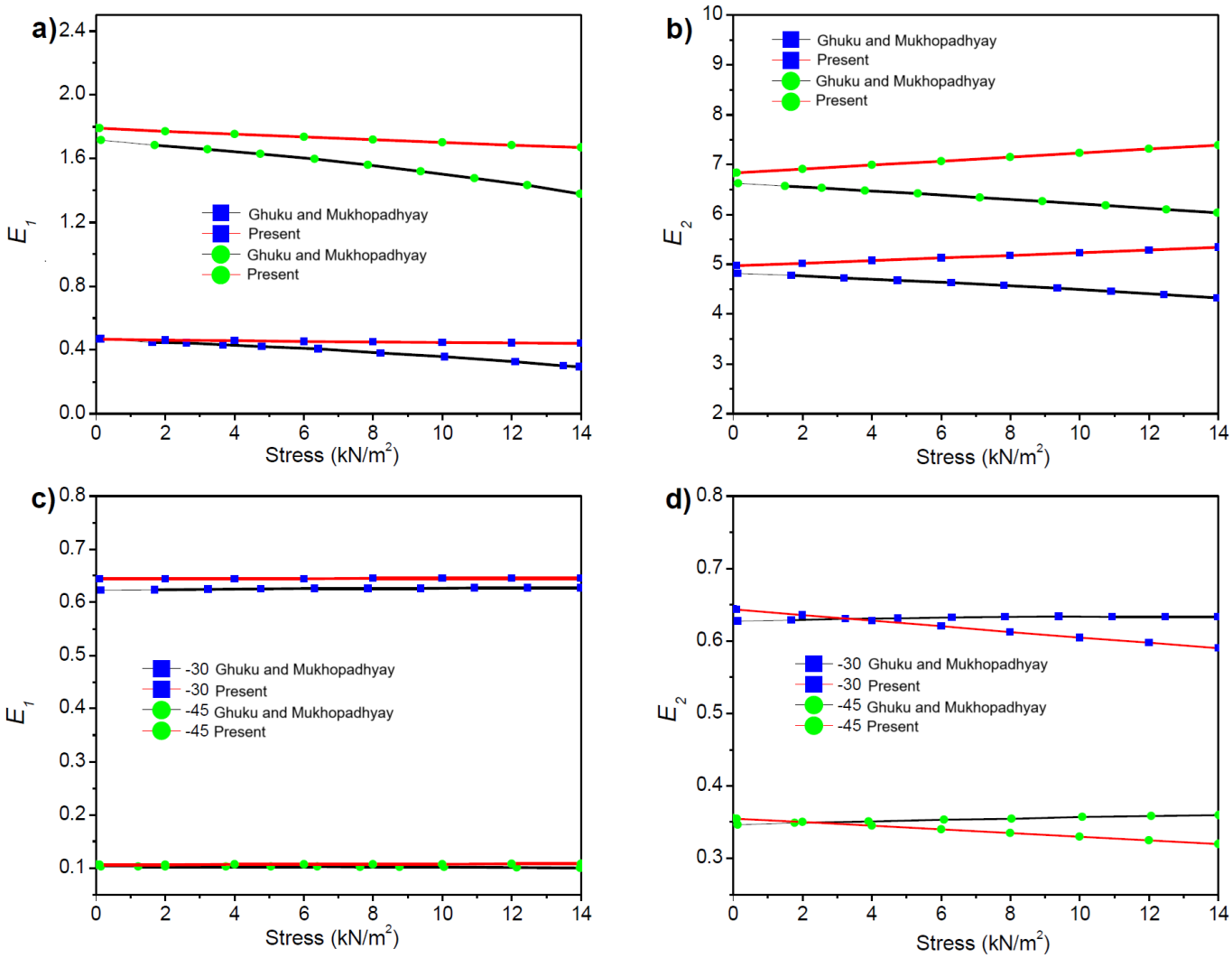

Figure 7: Validation of nonlinear in-plane effective material properties of straight isotropic lattice metamaterials. **(a)** Non-dimensional longitudinal elastic modulus E_1 of straight isotropic hexagonal lattice metamaterials under different stresses. **(b)** Non-dimensional transverse elastic modulus E_2 of straight isotropic hexagonal lattice metamaterials for different stresses. **(c)** Non-dimensional longitudinal elastic modulus E_1 of straight isotropic auxatic lattice metamaterials under different stresses. **(d)** Non-dimensional transverse elastic modulus E_2 of straight isotropic hexagonal lattice metamaterials for different stresses.

4.2. Computational results on effective elastic moduli

This section presents a computational study to investigate the influence of transverse beam curvature on the nonlinear in-plane and out-of-plane effective material properties of non-auxetic and auxetic functionally graded lattice metamaterials. We examine the effects of various influencing parameters, including: (a) Radius of curvature, (b) Cell angle, (c) Volume fraction index of the functionally graded beams, and (d) Applied stresses. By systematically varying these parameters, we aim to gain a comprehensive understanding of how curvature affects the mechanical response of these novel functionally graded metamaterials.

Table 2: Linear in-plane elastic modulus E_1 (MPa) of functionally graded curved lattice metamaterials.

Volume fraction	Cell angle	R_X/W			
		0.55	0.8	1	2
0	-45	5.0385	1.9280	1.3142	0.6269
	45	2.3594	0.9111	0.6226	0.2983
	-30	10.5107	4.0432	2.7600	1.3202
	30	6.0984	2.3821	1.6332	0.7870
1	-45	4.5441	1.7452	1.1948	0.5809
	45	2.3594	0.9111	0.6226	0.2983
	-30	9.4792	3.6598	2.5092	1.2233
	30	5.5002	2.1563	1.4848	0.7292
5	-45	3.6549	1.4112	0.9722	0.4853
	45	1.7116	0.6669	0.4606	0.2309
	-30	7.6240	2.9593	2.0418	1.0219
	30	4.4239	1.7435	1.2081	0.6091

Table 3: Linear in-plane elastic modulus E_2 (MPa) of functionally graded curved lattice metamaterials.

Volume fraction	cell angle	R_X/W			
		0.55	0.8	1	2
0	-45	16.5003	6.3861	4.3654	2.0901
	45	33.8893	13.2317	9.0675	4.3597
	-30	10.5616	4.0608	2.7709	1.3231
	30	17.4047	6.7267	4.5967	2.2003
1	-45	14.8767	5.7797	3.9683	1.9365
	45	30.5556	11.9753	8.2426	4.0394
	-30	9.5235	3.6755	2.5190	1.2259
	30	15.6942	6.0884	4.1788	2.0387
5	-45	11.9603	4.6726	3.2285	1.6173
	45	24.5663	9.6812	6.7059	3.3736
	-30	7.6577	2.9717	2.0495	1.0239
	30	12.6198	4.9225	3.4000	1.7028

4.2.1. Linear characterization of effective elastic moduli

We investigate the effect of beam curvature on functionally graded lattice metamaterials in the small-deformation linear regime, as shown in Tables 2 - 9. The material properties for the metal component are: Young's modulus (E) = 210 GPa, density (ρ) = 8166 kg/m^3, and Poisson's ratio (ν) = 0.3. The ceramic component has the following properties: E = 380 GPa, ρ = 3960 kg/m^3, and ν = 0.3. For the honeycomb cell, the slanted beam length (l) is 18.35 mm, the vertical beam length (h) is 36.7 mm, the beam width is 2 mm and the thickness is 0.1835 mm. The parametric study of the nonlinear functionally graded lattice metamaterial considers four cell angles (-45°, -30°, 30°, 45°) and four radius of curvatures along the transverse direction (R_x/W = 0.55, 0.8, 1, 2). Tables 2, 3, and 5 present

Table 4: Linear out of plane elastic modulus E_3 (MPa) of functionally graded curved lattice metamaterials.

Volume fraction	cell angle	R_X/W			
		0.55	0.8	1	2
0	-45	95.025	347.383	603.938	2309.510
	45	45.383	165.908	288.436	1103.004
	-30	66.876	244.478	425.034	1625.363
	30	40.126	146.688	255.023	975.224
1	-45	89.113	326.468	566.912	2143.827
	45	42.560	155.918	270.753	1023.875
	-30	62.714	229.755	398.971	1508.744
	30	37.629	137.853	239.383	905.247
5	-45	75.605	277.641	481.244	1790.852
	45	36.109	132.599	229.838	855.297
	-30	53.208	195.393	338.681	1260.333
	30	31.925	117.236	203.209	756.200

Table 5: Linear in-plane shear modulus G_{12} (MPa) of functionally graded curved lattice metamaterials.

Volume fraction	cell angle	R_X/W			
		0.55	0.8	1	2
0	-45	6.35945	0.64989	0.35816	0.13142
	45	0.72988	0.24365	0.15947	0.07161
	-30	1.67351	0.36603	0.21907	0.08775
	30	0.88736	0.27135	0.17370	0.07561
1	-45	5.30167	0.57599	0.32101	0.12121
	45	0.65535	0.21971	0.14454	0.06628
	-30	1.47579	0.32717	0.19734	0.08105
	30	0.79460	0.24425	0.15723	0.06994
5	-45	3.86129	0.45304	0.25639	0.10064
	45	0.52389	0.17676	0.11714	0.05528
	-30	1.15171	0.26018	0.15864	0.06741
	30	0.63289	0.19604	0.12720	0.05830

the in-plane material properties of the curved lattice metamaterial in the linear regime. The effective elastic moduli are observed to increase with decreasing radius of curvature. This phenomenon can be attributed to the reduced beam deflection caused by the introduction of curvature in the beam's cross-section compared to a straight beam. The curvature effectively stiffens the beam, leading to a higher resistance to bending. This effect is more pronounced for beams with a smaller radius of curvature (i.e., more curved beams). As the mathematical formulations demonstrate, effective in-plane material properties are inversely proportional to the beam deflections in the considered bending dominated honeycomb lattices. Therefore, by strategically incorporating curvature into the beam cross-sections, we can tailor the effective in-plane material properties of the lattice metamaterial to achieve desired level of high specific stiffness. It is important to note that the relationship between the change in radius

Table 6: Linear out-of-plane shear modulus G_{23} (MPa) of functionally graded curved lattice metamaterials.

Volume fraction	cell angle	R_X/W			
		0.55	0.8	1	2
0	-45	923.43	1528.93	1817.17	2435.76
	45	441.02	730.20	867.87	1163.30
	-30	397.95	652.46	769.90	1012.25
	30	238.77	391.47	461.94	607.35
1	-45	837.51	1381.16	1636.60	2175.71
	45	399.99	659.63	781.63	1039.10
	-30	491.17	810.01	959.81	1275.99
	30	294.70	486.00	575.89	765.59
5	-45	678.56	1112.52	1312.77	1726.02
	45	324.07	531.33	626.97	824.33
	-30	541.56	896.67	1065.71	1428.50
	30	324.94	538.00	639.43	857.10

Table 7: Linear out-of-plane shear modulus G_{13} (MPa) of functionally graded curved lattice metamaterials.

Volume fraction	cell angle	R_X/W			
		0.55	0.8	1	2
0	-45	307.809	509.642	605.724	811.922
	45	147.007	243.401	289.289	387.767
	-30	324.937	538.000	639.429	857.099
	30	194.962	322.800	383.657	514.260
1	-45	279.170	460.387	545.534	725.237
	45	133.329	219.877	260.543	346.368
	-30	294.704	486.004	575.889	765.591
	30	176.822	291.603	345.533	459.355
5	-45	226.186	370.840	437.592	575.339
	45	108.025	177.110	208.990	274.778
	-30	238.772	391.474	461.940	607.353
	30	143.263	234.885	277.164	364.412

of curvature and the resulting change in material properties is not linear. The most significant increases in in-plane properties occur at lower radius of curvature values. Since this study focuses on beams with low curvature, the results presented here exclude data for beams with a high radius of curvature. However, the trend extends to these high curvature values; the material properties gradually converge towards those of a straight beam as the radius of curvature approaches infinity. The cell angle exhibits a noticeable influence on the various in-plane effective material properties. For Young's modulus in the direction 1, the lattice with a cell angle of -30° demonstrates the highest value, followed by the lattice with a 30° angle. Conversely, the lattice with a 45° cell angle exhibits the lowest. This trend is reversed when considering Young's modulus in direction 2 and the in-plane shear modulus. Here, the lattice with a 45° cell angle shows the highest values, followed by the 30° angle. The lattice with a -30° cell

Table 8: Linear in-plane Poisson's ratio ν_{12} of functionally graded curved lattice metamaterials.

Volume fraction	cell angle	R_X/W			
		0.55	0.8	1	2
0	-45	-0.54692	-0.54692	-0.54692	-0.54692
	45	0.26120	0.26120	0.26120	0.26120
	-30	-0.97936	-0.98888	-0.99148	-0.99592
	30	0.57769	0.58712	0.58997	0.59511
1	-45	-0.54692	-0.54692	-0.54692	-0.54692
	45	0.26120	0.26120	0.26120	0.26120
	-30	-0.97935	-0.98886	-0.99147	-0.99592
	30	0.57766	0.58709	0.58995	0.59510
5	-45	-0.54692	-0.54692	-0.54692	-0.54692
	45	0.26120	0.26120	0.26120	0.26120
	-30	-0.97934	-0.98884	-0.99145	-0.99591
	30	0.57763	0.58704	0.58991	0.59508

Table 9: Linear in-plane Poisson's ratio ν_{21} of functionally graded curved lattice metamaterials.

Volume fraction	cell angle	R_X/W			
		0.55	0.8	1	2
0	-45	-1.7911	-1.8115	-1.8168	-1.8233
	45	3.7517	3.7934	3.8042	3.8178
	-30	-1.0062	-1.0047	-1.0041	-1.0021
	30	1.7062	1.6923	1.6875	1.6771
1	-45	-1.7905	-1.8112	-1.8165	-1.8232
	45	3.7506	3.7928	3.8037	3.8174
	-30	-1.0060	-1.0046	-1.0040	-1.0021
	30	1.7059	1.6922	1.6874	1.6770
5	-45	-1.7897	-1.8108	-1.8162	-1.8229
	45	3.7489	3.7920	3.8031	3.8168
	-30	-1.0057	-1.0045	-1.0039	-1.0020
	30	1.7055	1.6920	1.6873	1.6769

angle exhibits the lowest transverse Young's modulus and in-plane shear modulus. Interestingly, this behavior is consistent for both h/l ratios (1 and 2).

The out-of-plane material properties exhibit an opposite trend compared to their in-plane counterparts. This is because they are primarily governed by out-of-plane deflections, which increase with the introduction of curvature in the beams. Consequently, the out-of-plane properties of the lattice metamaterials decrease. Notably, the out-of-plane properties of lattices with conventional straight beams are significantly higher than their in-plane properties. Such disparity is reduced with the introduction of curvature. This ability to tailor both sets of properties (in-plane and out-of-plane) unlocks the full potential of lattice metamaterials for applications where both in-plane and out-of-plane mechanical responses are crucial. The out-of-plane material properties are presented in Tables 4, 6, and 7. In

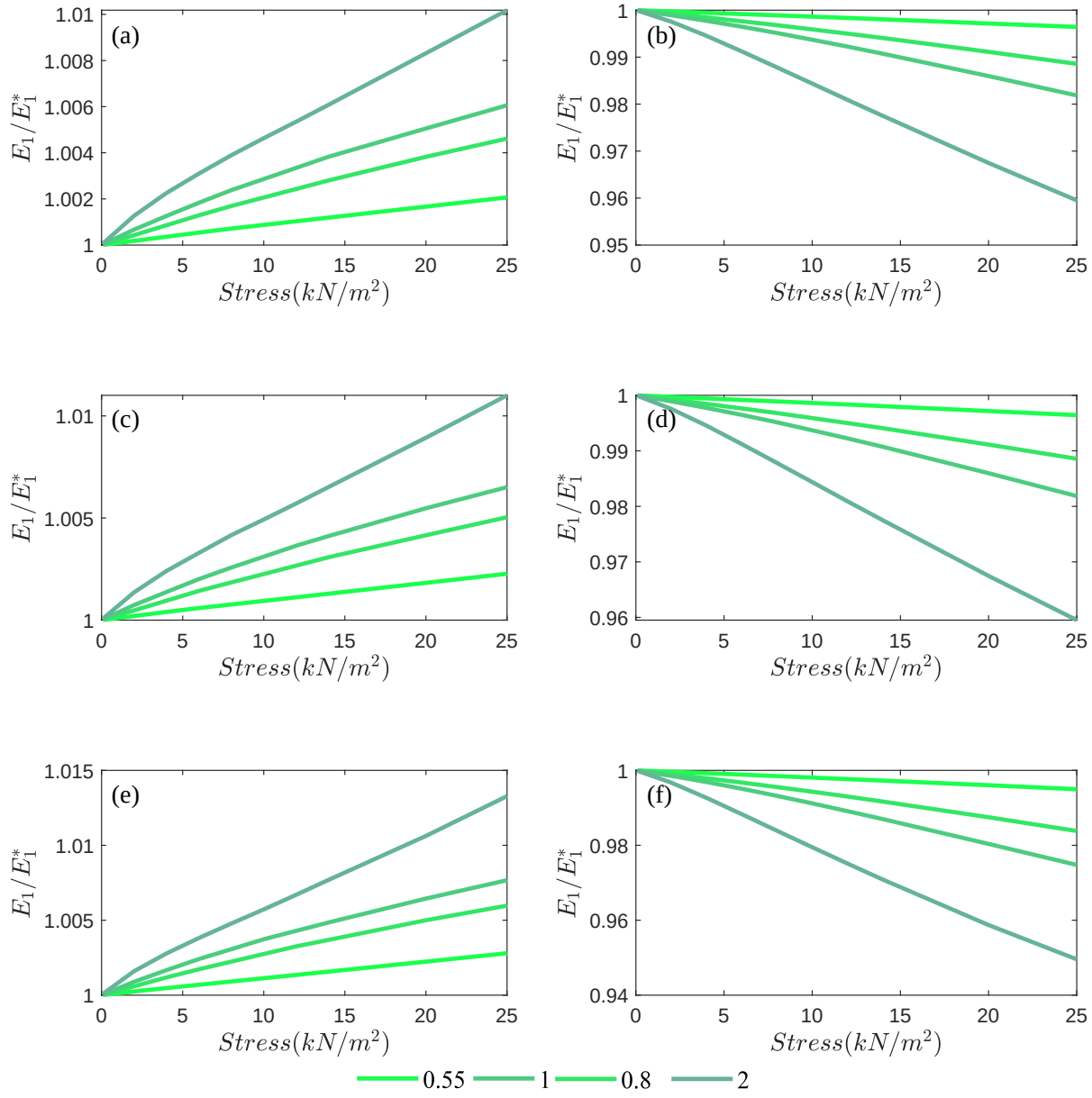

Figure 8: Non-linear effective Young's modulus (E_1) of transversely curved functionally graded metamaterials. **(a)** E_1 of curved isotropic lattice metamaterials for cell angle -30^o (Auxetic configuration). **(b)** E_1 of curved isotropic lattice metamaterials for cell angle 30^o (Non-auxetic configuration). **(c)** E_1 of curved functionally graded lattice metamaterials with volume fraction index 1 and cell angle -30^o (Auxetic configuration). **(d)** E_1 of curved functionally graded lattice metamaterials with volume fraction index 1 and cell angle 30^o (Non-auxetic configuration). **(e)** E_1 of curved functionally graded lattice metamaterials with volume fraction index 5 and cell angle -30^o (Auxetic configuration). **(f)** E_1 of curved functionally graded lattice metamaterials with volume fraction index 5 and cell angle 30^o (Non-auxetic configuration). The colour gradation represents transverse curvature here.

contrast to the observed variations in the in-plane properties, the influence of the cell angle on the out-of-plane properties is consistent. Here, auxetic lattices exhibit significantly higher out-of-plane material properties compared to non-auxetic lattices. Furthermore, we observe a trend where lower cell angles correspond to higher out-of-plane moduli. This trend can be attributed to the dependence of

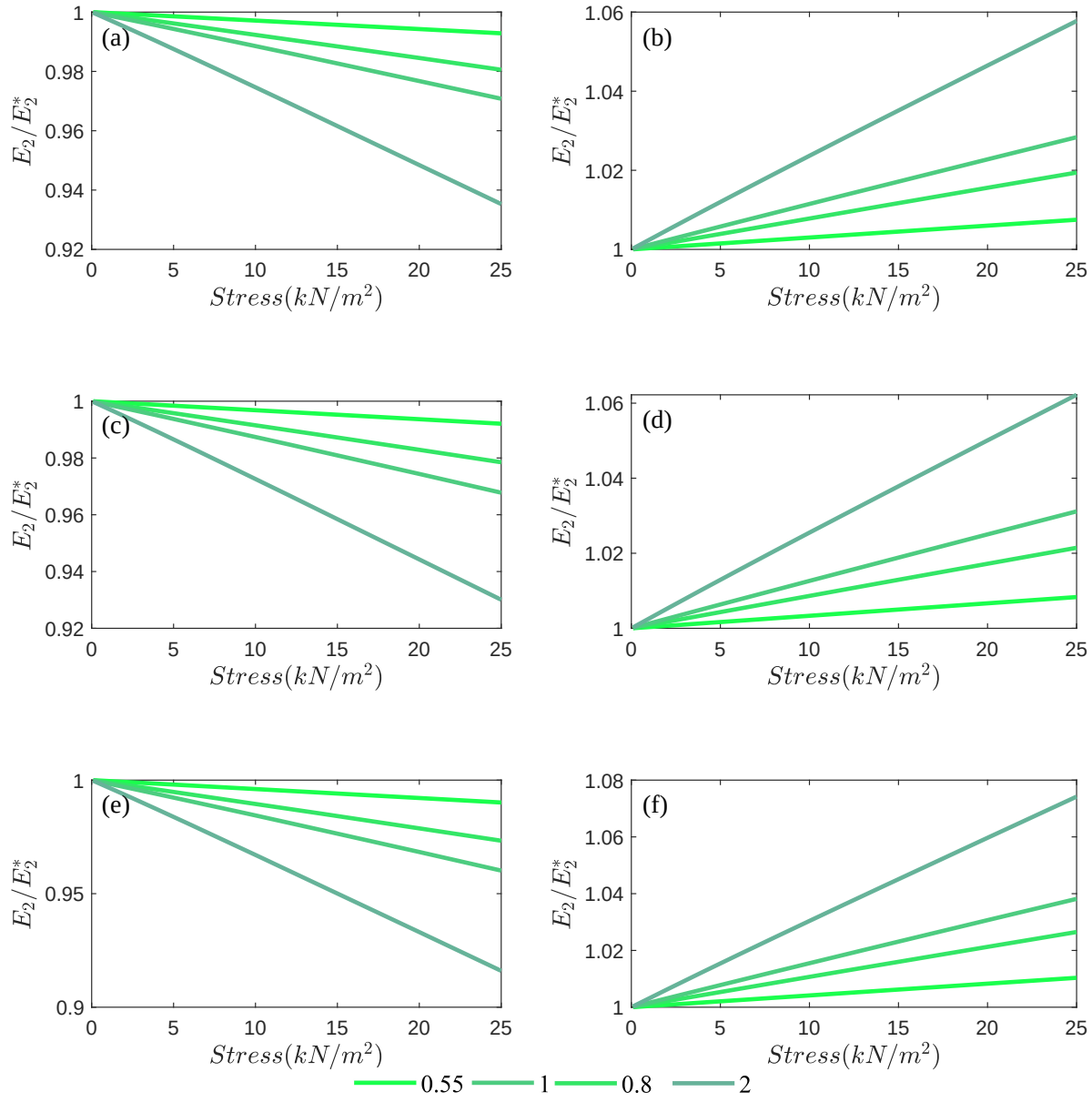

Figure 9: Non-linear effective Young's modulus (E_2) of transversely curved functionally graded metamaterials. **(a)** E_2 of curved isotropic lattice metamaterials for cell angle -30^o (Auxetic configuration). **(b)** E_2 of curved isotropic lattice metamaterials for cell angle 30^o (Non-auxetic configuration). **(c)** E_2 of curved functionally graded lattice metamaterials with volume fraction index 1 and cell angle -30^o (Auxetic configuration). **(d)** E_2 of curved functionally graded lattice metamaterials with volume fraction index 1 and cell angle 30^o (Non-auxetic configuration). **(e)** E_2 of curved functionally graded lattice metamaterials with volume fraction index 5 and cell angle -30^o (Auxetic configuration). **(f)** E_2 of curved functionally graded lattice metamaterials with volume fraction index 5 and cell angle 30^o (Non-auxetic configuration). The colour gradation represents transverse curvature here.

out-of-plane properties on cell volume. Lower cell angles result in denser lattices, which translates to lower overall cell volume. Denser packing leads to increased out-of-plane stiffness.

The volume fraction index exhibits a well-defined impact on the material properties of the functionally graded (FG) metamaterial. As the volume fraction index increases, all effective material properties

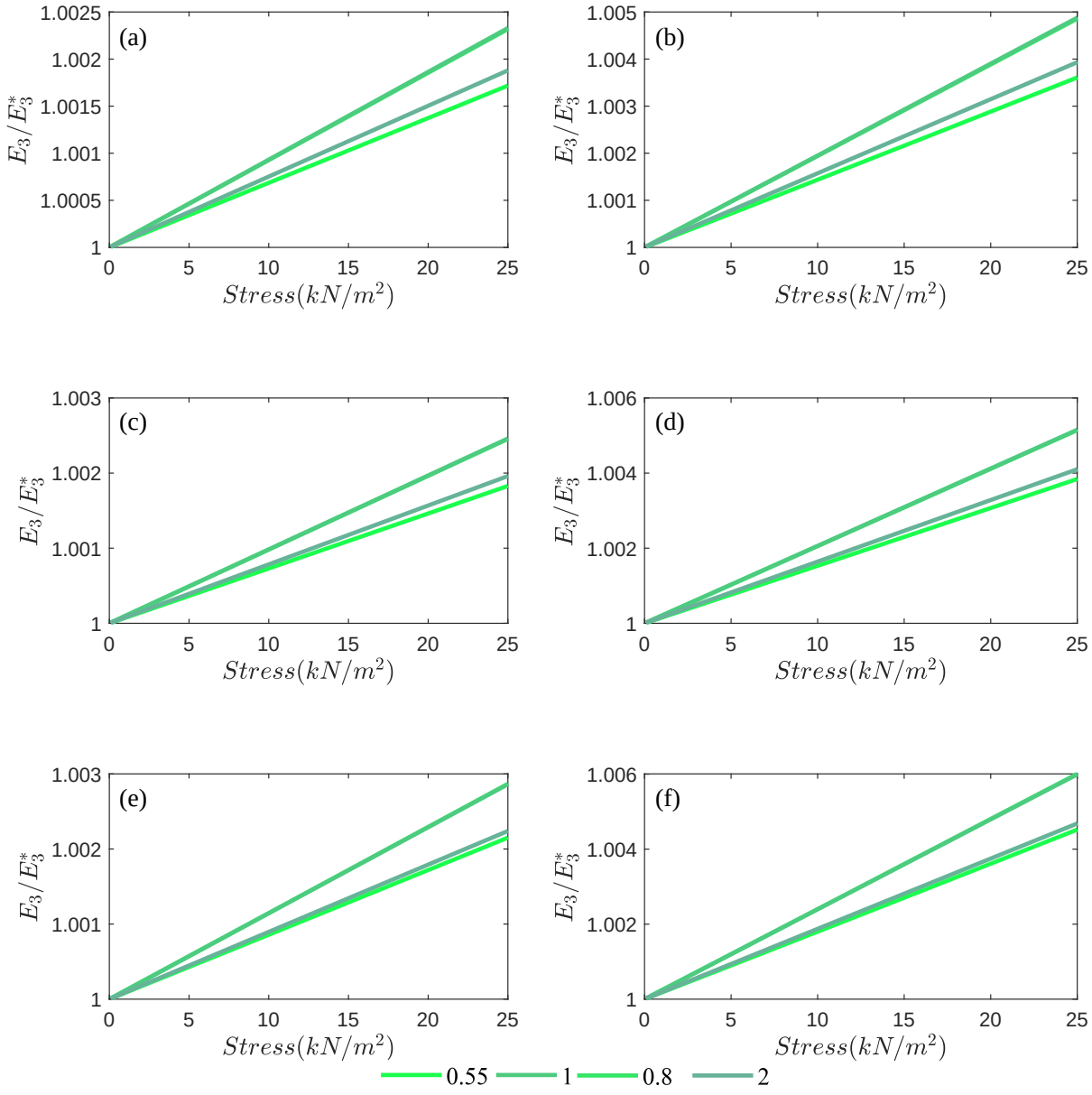

Figure 10: Non-linear effective Young's modulus (E_3) of transversely curved functionally graded metamaterials. **(a)** E_3 of curved isotropic lattice metamaterials for cell angle -30^o (Auxetic configuration). **(b)** E_3 of curved isotropic lattice metamaterials for cell angle 30^o (Non-auxetic configuration). **(c)** E_3 of curved functionally graded lattice metamaterials with volume fraction index 1 and cell angle -30^o (Auxetic configuration). **(d)** E_3 of curved functionally graded lattice metamaterials with volume fraction index 1 and cell angle 30^o (Non-auxetic configuration). **(e)** E_3 of curved functionally graded lattice metamaterials with volume fraction index 5 and cell angle -30^o (Auxetic configuration). **(f)** E_3 of curved functionally graded lattice metamaterials with volume fraction index 5 and cell angle 30^o (Non-auxetic configuration). The colour gradation represents transverse curvature here.

decrease. This behavior can be explained by considering the change in the composition of the material within the FG beam. With a higher volume fraction index, the beam's behavior becomes more akin to that of the metal component due to its increased volume fraction within the composite. Since the metal component generally has a lower stiffness compared to the ceramic component, the overall stiffness of

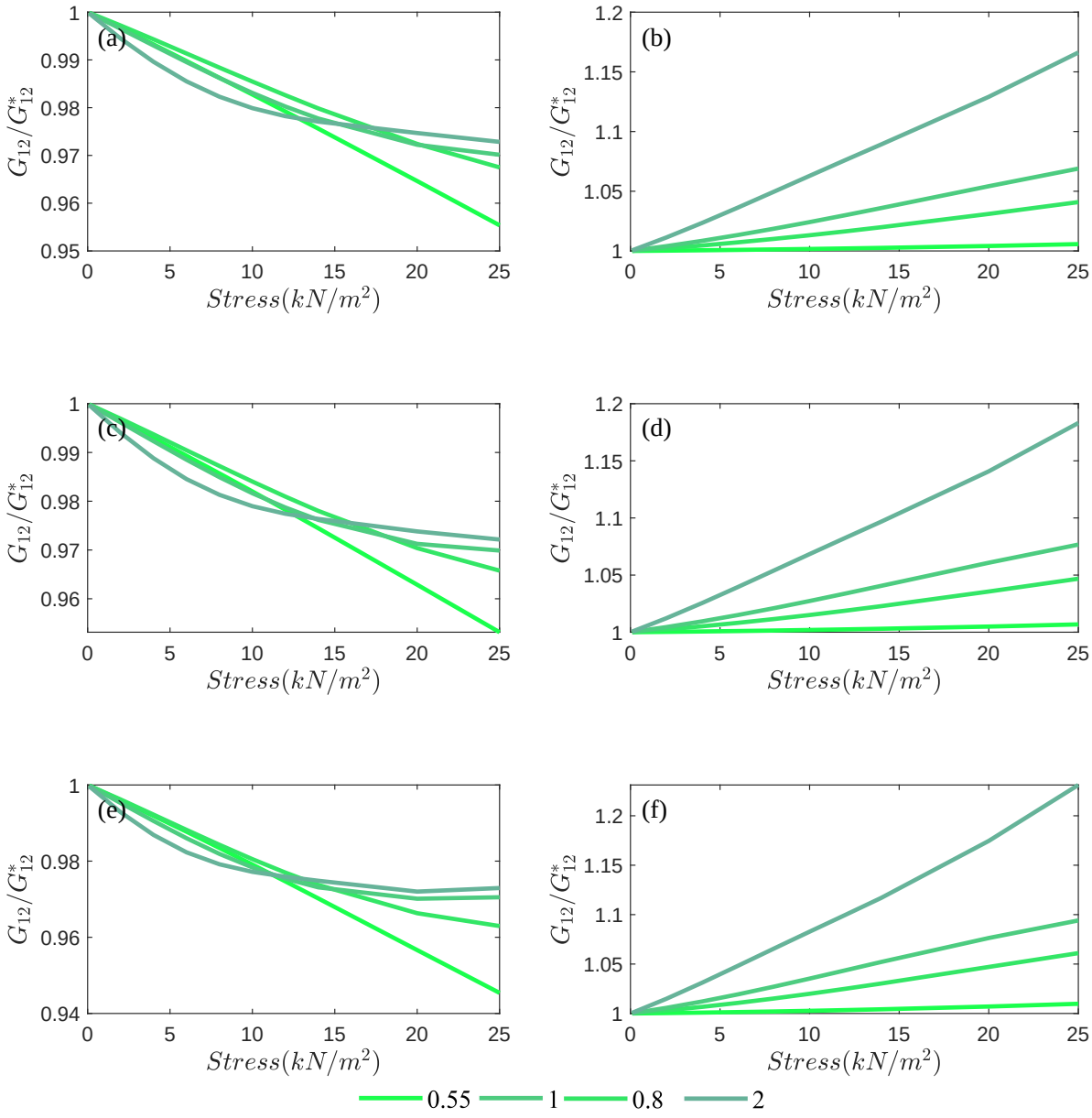

Figure 11: Non-linear effective shear modulus (G_{12}) **of transversely curved functionally graded metamaterials. (a)** (G_{12}) of curved isotropic lattice metamaterials for cell angle -30^o (Auxetic configuration). **(b)** (G_{12}) of curved isotropic lattice metamaterials for cell angle 30^o (Non-auxetic configuration). **(c)** (G_{12}) of curved functionally graded lattice metamaterials with volume fraction index 1 and cell angle -30^o (Auxetic configuration). **(d)** (G_{12}) of curved functionally graded lattice metamaterials with volume fraction index 1 and cell angle 30^o (Non-auxetic configuration). **(e)** (G_{12}) of curved functionally graded lattice metamaterials with volume fraction index 5 and cell angle -30^o (Auxetic configuration). **(f)** (G_{12}) of curved functionally graded lattice metamaterials with volume fraction index 5 and cell angle 30^o (Non-auxetic configuration). The colour gradation represents transverse curvature here.

the FG beam decreases. Interestingly, neither the volume fraction index nor the radius of curvature of the beam significantly affect the in-plane Poisson ratios (ν_{12} and ν_{12}) of FG metamaterial.

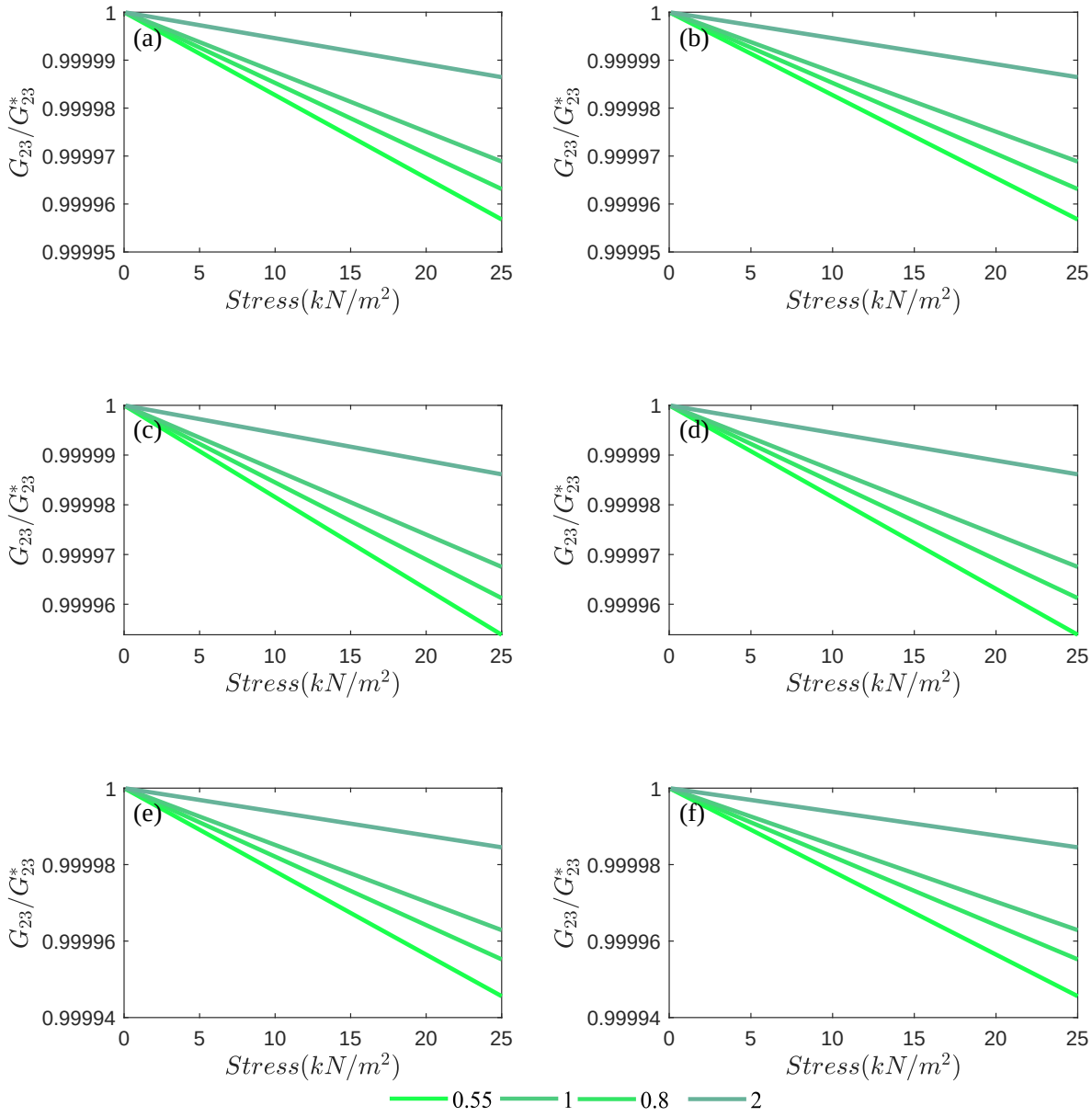

Figure 12: Non-linear effective shear modulus (G_{23}) of transversely curved functionally graded metamaterials. (a) (G_{23}) of curved isotropic lattice metamaterials for cell angle -30^o (Auxetic configuration). **(b)** (G_{23}) of curved isotropic lattice metamaterials for cell angle 30^o (Non-auxetic configuration). **(c)** (G_{23}) of curved functionally graded lattice metamaterials with volume fraction index 1 and cell angle -30^o (Auxetic configuration). **(d)** (G_{23}) of curved functionally graded lattice metamaterials with volume fraction index 1 and cell angle 30^o (Non-auxetic configuration). **(e)** (G_{23}) of curved functionally graded lattice metamaterials with volume fraction index 5 and cell angle -30^o (Auxetic configuration). **(f)** (G_{23}) of curved functionally graded lattice metamaterials with volume fraction index 5 and cell angle 30^o (Non-auxetic configuration). The colour gradation represents transverse curvature here.

4.2.2. Nonlinear characterization of effective elastic moduli

We now investigate the material properties of functionally graded (FG) metamaterials under various loading conditions incorporating geometric nonlinearity. The material properties for the metal and ceramic components remain the same as in the previous section. For the honeycomb cell, the slanted

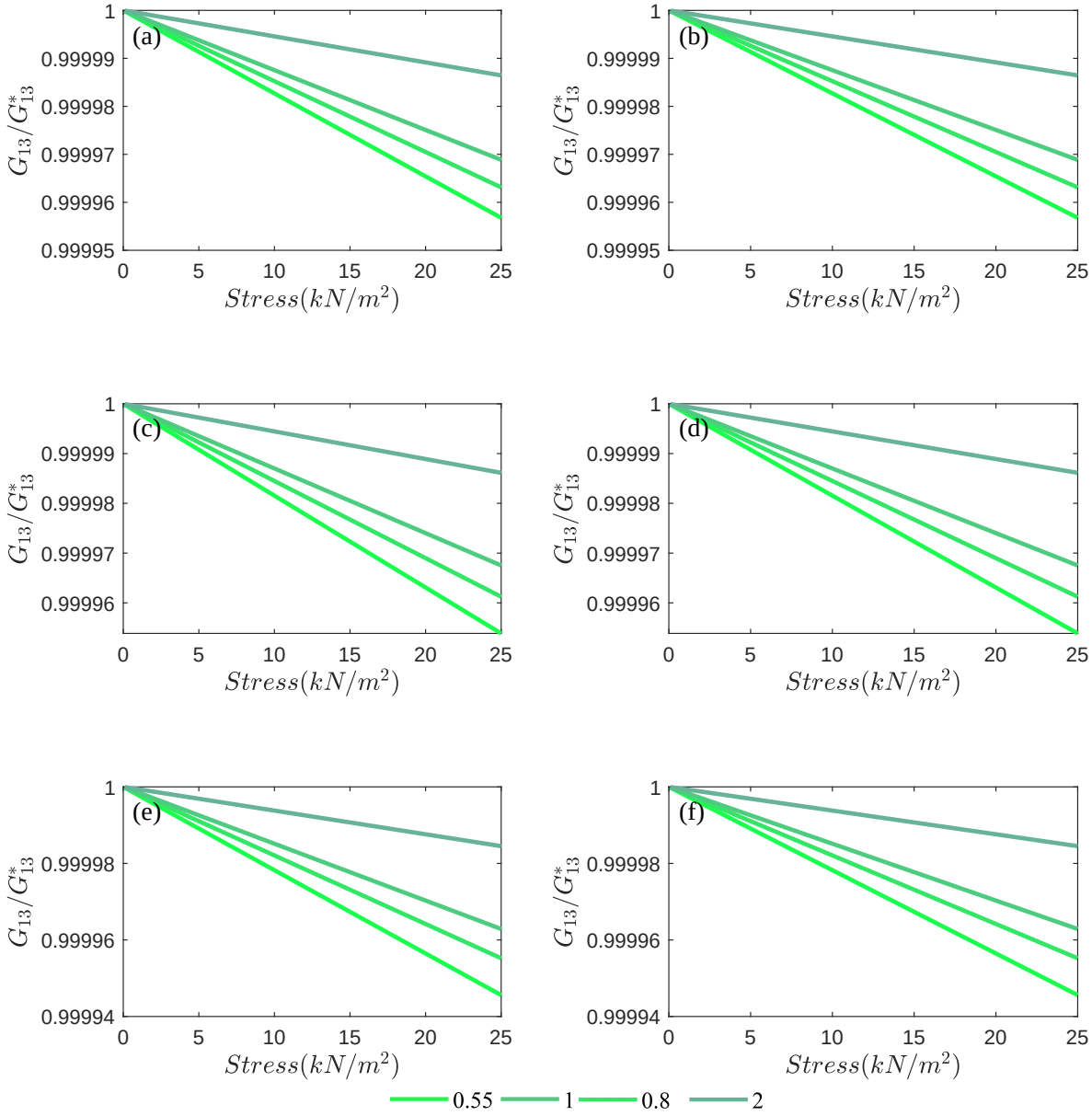

Figure 13: Non-linear effective shear modulus (G_{13}) **of transversely curved functionally graded metamaterials. (a)** (G_{13}) of curved isotropic lattice metamaterials for cell angle -30^o (Auxetic configuration). **(b)** (G_{13}) of curved isotropic lattice metamaterials for cell angle 30^o (Non-auxetic configuration). **(c)** (G_{13}) of curved functionally graded lattice metamaterials with volume fraction index 1 and cell angle -30^o (Auxetic configuration). **(d)** (G_{13}) of curved functionally graded lattice metamaterials with volume fraction index 1 and cell angle 30^o (Non-auxetic configuration). **(e)** (G_{13}) of curved functionally graded lattice metamaterials with volume fraction index 5 and cell angle -30^o (Auxetic configuration). **(f)** (G_{13}) of curved functionally graded lattice metamaterials with volume fraction index 5 and cell angle 30^o (Non-auxetic configuration). The colour gradation represents transverse curvature here.

beam length (l) is 18.35 mm, the vertical beam length (h) is 36.7 mm, the beam width is 2 mm and the thickness is 0.1835 mm. The parametric study of the nonlinear functionally graded lattice metamaterial considers two cell angles (-30° and 30°), four radius of curvatures along the transverse direction (R_x/W = 0.55, 0.8, 1, 2), and eleven stress values (0.001, 0.1, 2, 4, 6, 8, 10, 12, 14, 20, 25 kN/m^2). By incorporating

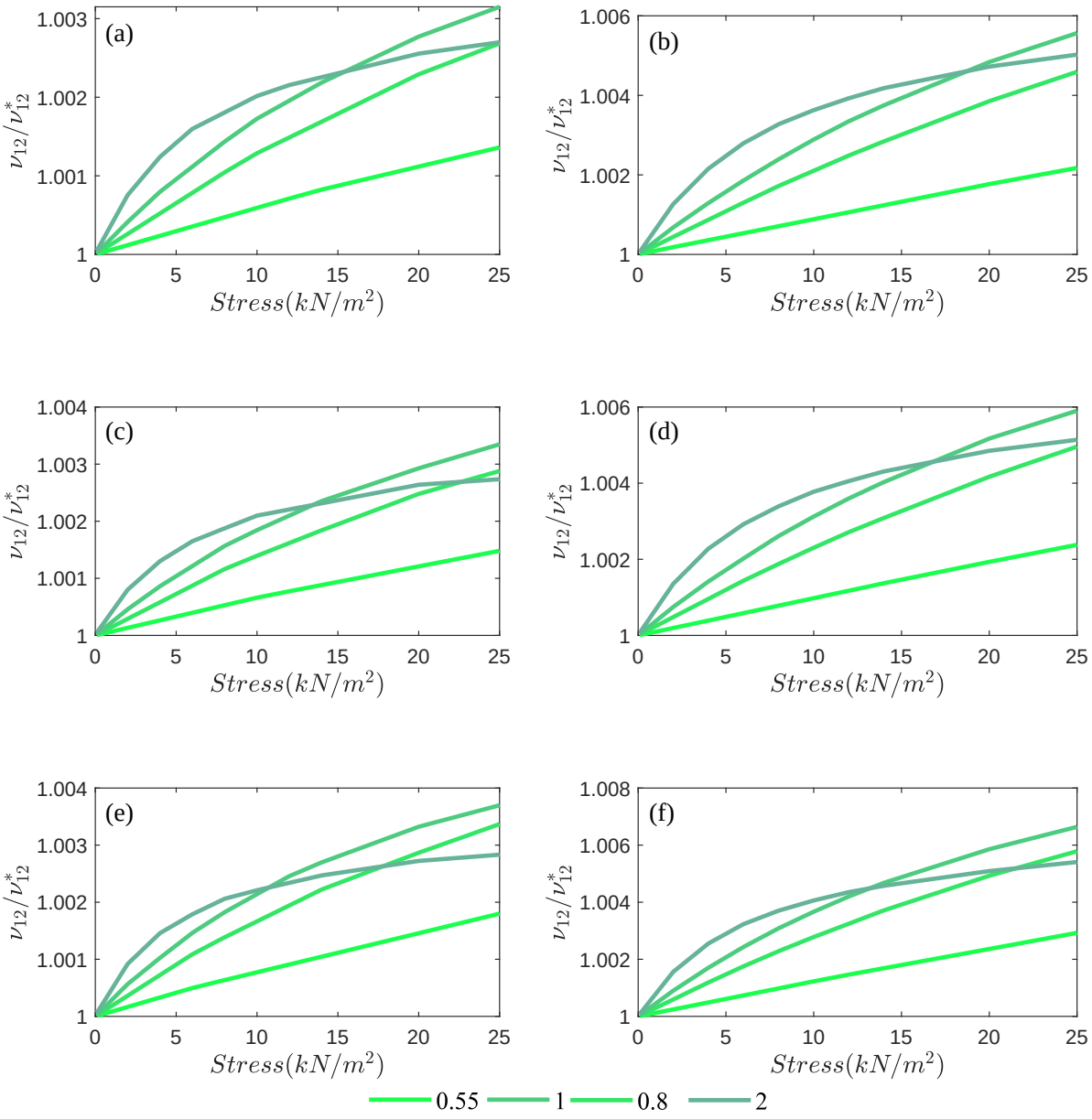

Figure 14: Non-linear effective Poisson's ratio (ν_{12}) of transversely curved functionally graded metamaterials. **(a)** (ν_{12}) of curved isotropic lattice metamaterials for cell angle -30^o (Auxetic configuration). **(b)** (ν_{12}) of curved isotropic lattice metamaterials for cell angle 30^o (Non-auxetic configuration). **(c)** (ν_{12}) of curved functionally graded lattice metamaterials with volume fraction index 1 and cell angle -30^o (Auxetic configuration). **(d)** (ν_{12}) of curved functionally graded lattice metamaterials with volume fraction index 1 and cell angle 30^o (Non-auxetic configuration). **(e)** (ν_{12}) of curved functionally graded lattice metamaterials with volume fraction index 5 and cell angle -30^o (Auxetic configuration). **(f)** (ν_{12}) of curved functionally graded lattice metamaterials with volume fraction index 5 and cell angle 30^o (Non-auxetic configuration). The colour gradation represents transverse curvature here.

geometric nonlinearity, this study aims to capture the behavior of the metamaterial under more realistic loading conditions, where large deformations may occur. The results presented for this study are in terms of non-dimensional material properties. These are calculated as the ratio of the nonlinear property to the corresponding linear property of the material ($E_1^*, E_2^*, E_3^*, G_{12}^*, G_{13}^*, G_{23}^*, \nu_{12}, \nu_{21}$). The linear small-

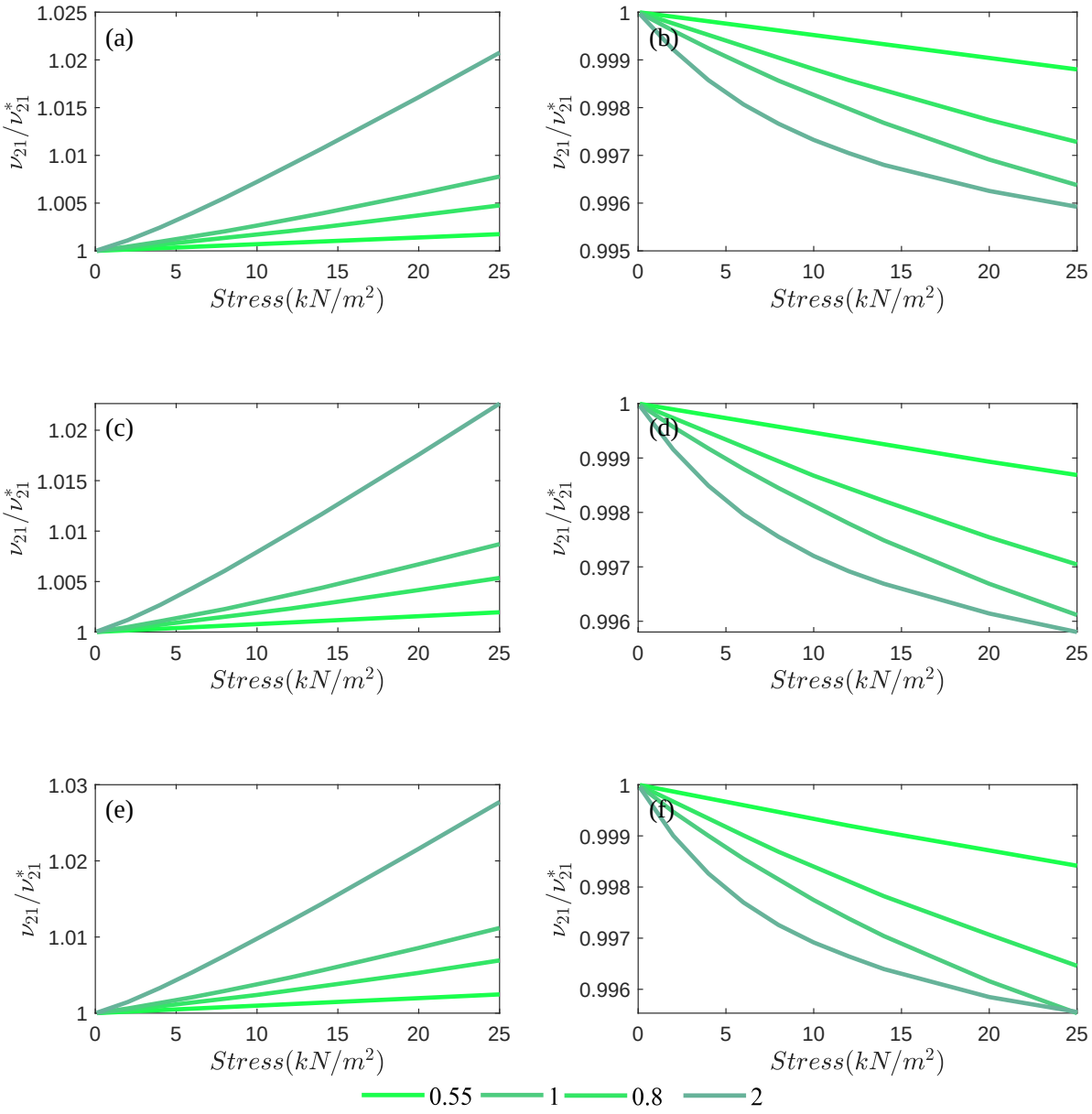

Figure 15: Non-linear effective Poisson's ratio (ν_{21}) of transversely curved functionally graded metamaterials. **(a)** (ν_{21}) of curved isotropic lattice metamaterials for cell angle -30^o (Auxetic configuration). **(b)** (ν_{21}) of curved isotropic lattice metamaterials for cell angle 30^o (Non-auxetic configuration). **(c)** (ν_{21}) of curved functionally graded lattice metamaterials with volume fraction index 1 and cell angle -30^o (Auxetic configuration). **(d)** (ν_{21}) of curved functionally graded lattice metamaterials with volume fraction index 1 and cell angle 30^o (Non-auxetic configuration). **(e)** (ν_{21}) of curved functionally graded lattice metamaterials with volume fraction index 5 and cell angle -30^o (Auxetic configuration). **(f)** (ν_{21}) of curved functionally graded lattice metamaterials with volume fraction index 5 and cell angle 30^o (Non-auxetic configuration). The colour gradation represents transverse curvature here.

deformation properties of the lattice material are provided in Tables 2 to 9.

Our analysis reveals contrasting behavior in in-plane Young's modulus (E_1) for non-auxetic and auxetic metamaterials under increasing load (see Fig. 8). For non-auxetic metamaterials, E_1 exhibits a positive correlation with load, indicating a stiffening effect. Conversely, auxetic metamaterials display

a decrease in E_1 with increasing load, suggesting a softening response. Interestingly, the radius of curvature in the beams plays a crucial role. Higher curvature beams exhibit a more pronounced deviation in E_1 under load, with non-auxetic structures stiffening even further and auxetic structures softening more significantly compared to their lower curvature counterparts. The influence of the volume fraction index on E_1 remains consistent with the observations of the linear analysis.

The behavior of the other in-plane Young's modulus, E_2, under increasing load presents a fascinating contrast to E_1 as shown in Fig. 9. Here, we observe the opposite trends compared to those seen for E_1. Hexagonal metamaterials exhibit a softening effect, with E_2 decreasing as load increases. This indicates a decrease in resistance to deformation in direction 2 under load. Conversely, auxetic metamaterials display a stiffening response, with E_2 increasing as the load intensifies. This suggests that auxetic structures become more resistant to deformation in direction 2 under load. It is important to note that the influence of the volume fraction index on both E_1 and E_2 remains consistent with the observations from the linear analysis.

The out-of-plane Young's modulus, E_3, exhibits trends similar to in-plane E_1 under increasing load, but with less pronounced effects as seen in Fig. 10. Non-auxetic metamaterials show a stiffening response, with E_3 increasing slightly as the load intensifies. In contrast, auxetic metamaterials show a softening response, with E_3 decreasing slightly with increasing load. However, the magnitude of these changes in E_3 is significantly lower compared to the observed variations in E_1. Interestingly, the radius of curvature in the beams has minimal influence on the variation of E_3 under increasing load. This differs from the behavior of E_1, where curvature played a more significant role. The influence of the volume fraction index on E_3 remains consistent with the observations from the linear analysis.

The in-plane shear modulus, G_{12}, exhibits contrasting responses for non-auxetic and auxetic metamaterials under increasing load (see Fig. 11). Non-auxetic structures display a softening effect, with G_{12} decreasing as the load intensifies. This indicates a reduced resistance to shear deformation in the 1-2 plane under load. In contrast, auxetic metamaterials exhibit a pronounced stiffening response, with G_{12} increasing as the load intensifies. This suggests that auxetic structures become significantly more resistant to shear deformation under load, amplifying the trend observed for E_2. The influence of the radius of curvature on the change in the properties of the material becomes more complex with increasing load. The relationship between load and G_{12} transitions from linear to a more pronounced nonlinear behavior. For non-auxetic metamaterials, this change takes the form of a parabolic curve, while for auxetic metamaterials, it becomes exponential. This highlights the significant role of curvature in tailoring the response of the material under complex loading conditions.

The out-of-plane shear moduli, G_{23} and G_{13}, exhibit a distinct trend compared to all other properties of the material observed under increasing load, as seen in Figs. 12 and 13. Unlike the properties discussed previously, both non-auxetic and auxetic metamaterials show a decrease in G_{13} and G_{13} with increasing load. This suggests a weakening effect in resisting out-of-plane shear deformations. Furthermore, the magnitude of this decrease is significantly lower than that observed in other material properties. In fact, for higher radius of curvatures, the change in G_{13} and G_{13} becomes even less pronounced.

The Poisson ratio, ν_{12}, exhibits a fascinating response under increasing load, displaying an increase for non-auxetic and auxetic metamaterials, as shown in Fig. 14. This behavior suggests a coupling effect where deformation in direction 1 leads to a lateral contraction in direction 2, and this effect intensifies with increasing load. Interestingly, the relationship between the load and ν_{12} becomes progressively nonlinear. This transition takes the form of a parabolic curve for both material types, but with a slightly more pronounced effect observed for auxetic metamaterials compared to non-auxetic ones. This finding highlights the complex interplay between material properties under geometric nonlinearity, where the response of auxetic architectures deviates qualitatively from the non-auxetic ones.

Similar to the trends of in-plane Young's modulus (E_1), Poisson's ratio ν_{21} exhibits contrasting responses for non-auxetic and auxetic metamaterials under increasing load, as presented in Fig. 15. Non-auxetic structures display a positive correlation with load, indicating that ν_{21} increases as the load intensifies. In contrast, auxetic metamaterials exhibit a decrease in ν_{21} with increasing load. This suggests opposing effects on the coupling between deformations in directions 1 and 2 under load for these two classes of metamaterial architecture. Furthermore, the radius of curvature plays an important role. Higher curvature beams experience a more pronounced deviation in ν_{21} under load. This deviation becomes progressively nonlinear as the curvature increases, highlighting a complex interplay between material properties and geometry under large deformation. The influence of curvature becomes even more prominent for ν_{21} compared to E_1, suggesting a more nuanced relationship.

Fig. 16 presents the change in density of lattice metamaterials for various curvatures of beam, cell angle, and power law indices, as considered in this paper. It is observed that the density increases as the curvature of beam decreases. However, the increase in in-plane modulus due to curvature is much higher than the increase in the density; thus significantly improving the specific modulus of the lattice structures. It should also be noted that the density of the lattice metamaterials does not change significantly due to the effect of geometric nonlinearity.

In the proposed functionally graded metamaterials the outer sides of the constituting beams are rich in ceramic to shield the structure from extreme surrounding environmental effects, while the center

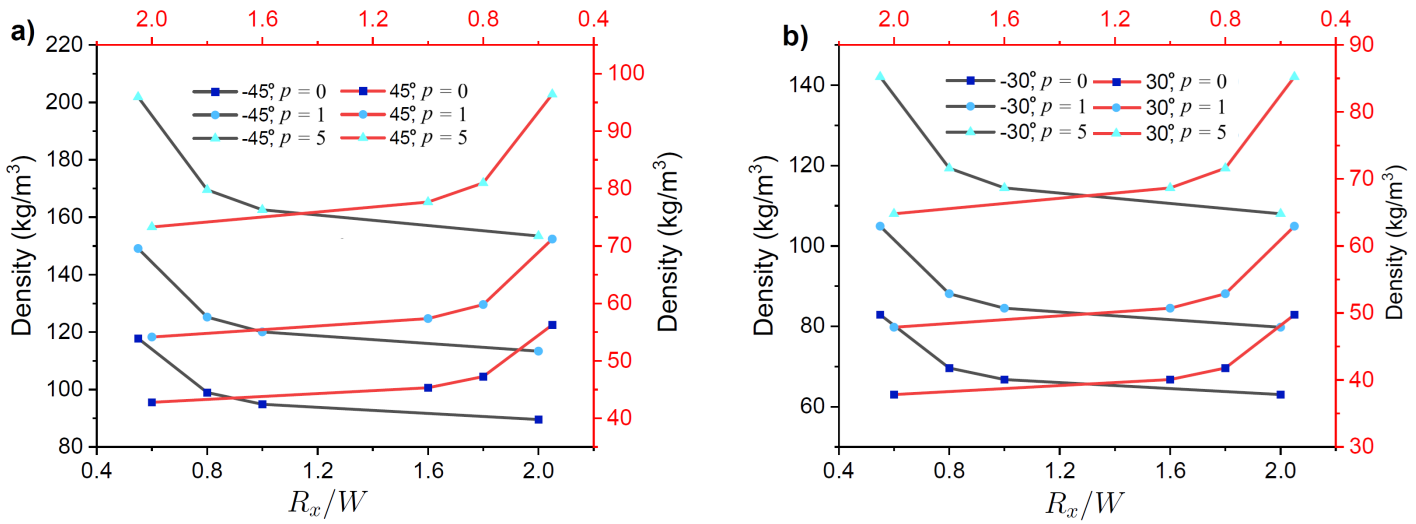

Figure 16: Density of curved functionally graded metamaterials. **(a)** Density of curved functionally graded lattice metamaterials considering cell angle -45^o (Auxetic configuration) and 45^o (Non-auxetic configuration) for various power law indices ($p = 0, 1, 5$). **(b)** Density of curved functionally graded lattice metamaterial considering cell angle -30^o (Auxetic configuration) and 30^o (Non-auxetic configuration) for various power law indices ($p = 0, 1, 5$).

part of the beam is rich in metal to enhance mechanical properties. Through this functionally graded architecture the onset of failure strength can be significantly increased as the high strength ceramic materials (note that failure strength of ceramic materials are normally much higher than metals [83]) are placed at the outer surfaces where the state of stress becomes most critical in bending dominated lattices. Due to these clear advantages, ceramic-metal-ceramic based functionally graded material is considered here, leading to multiple functionalities and behavioural versatility in terms of an adequate balance of ductility, stiffness, strength and resistance to adverse surrounding conditions.

The current paper focuses mainly on establishing the idea of functionally graded (across the thickness of cell walls) metamaterials and their stiffness (based on effective elastic properties). However, some of the other critical properties of such metamaterials are effective strength and energy absorption properties. Critical effective strength, defined by the onset of failure, can be effectively measured by analysing the beams based on appropriate failure criteria (considering both material failure and buckling) under the same periodic boundary and loading conditions explained in this paper. The energy absorption capability can be measured considering the area under the resultant force-displacement constitutive curve based on the identified point of onset of failure.

5. Conclusions and perspective

This article presents a semi-analytical computational model to predict the in-plane and out-of-plane nonlinear effective elastic properties of a new class of functionally graded lattice metamaterais with curved cell wall geometry. For nonlinear finite element modeling of the beam-like cell walls, accurate

degenerated shell elements are exploited, and subsequently the beam-level numerical results are integrated with unit cell mechanics following a nonlinear semi-analytical framework to obtain the effective elastic properties of the lattices. We envisage that the proposed functionally graded metamaterials can play a crucial role in developing futuristic hydrogen storage systems due to their remarkable tolerance towards extreme hot or cold environments and chemical surface degradation under extreme surrounding conditions.

We have proposed the next-generation concept design of hydrogen storage tanks with functionally graded metamaterial core for aerospace and automotive applications. The outer sides of the proposed constituting beams are rich in ceramic to shield the structure from extreme surrounding environmental effects, while the center part of the beam is rich in metal to enhance strength and stiffness. Based on such innovative lattice metamaterial based design of hydrogen storage tanks it is possible to enhance the storage capability in terms of internal pressure and resistance to external loads and impacts. Most importantly the proposed concept would lead to a breakthrough in developing load-bearing energy storage devices. For the proposed metamaterial core, the hexagonal bending-dominated unit cell architecture with transversely curved connecting beam-like geometries would ensure the dual functionality of high specific stiffness and energy absorption capability which are mutually exclusive in traditional lattice metamaterials.

We show that introduction of transverse curvature significantly increases the specific stiffness of the lattice metamaterials without any appreciable increase in weight. Under higher far-field stresses, the numerical results reveal a contrasting nonlinear behavior of softening and hardening depending on the unit cell architecture. This effect is further amplified in the presence of curvature, with higher curvatures leading to a more pronounced stiffening or softening. Interestingly, the influence of curvature is less significant for out-of-plane properties, where the effective material properties exhibit minimal changes with load. Note that the hardening behaviour of metamaterials will provide extra strength and stiffness, whereas the softening of metamaterials will provide improved impact resistance and energy absorption capabilities. The research also explores how Poisson's ratios, which quantify the coupling between deformations in different directions, respond to load. Here, we reveal a fascinating interplay between Poisson's ratios in the large-deformation regime, transverse curvature and applied far-field stresses. It is noted that the onset of failure strength can be significantly increased due to the adoption of functionally graded cell wall architecture where the high strength ceramic materials are placed at the critical outer surfaces.

In summary, this paper offers valuable insights on tailoring the mechanical properties of functionally

graded lattice metamaterials by strategically manipulating the beam-level and unit cell level geometric and gradation features for applications in extreme surrounding environments. These new class of metamaterials with incredibly stiff, strong, yet lightweight characteristics, capable of withstanding extreme surrounding environment, will open new avenues for pushing the traditional boundaries in a range of engineering applications, from automobiles and buildings to aircraft and space applications. Though we focus here primarily on hydrogen storage tanks, the proposed concept can be extended to developing metamatrials for other critical engineering scenarios such as rocket fuel tanks, external rocket components, heat shields for spacecraft, protective suits for firefighters, lightweight yet robust armor and equipment for volcanic exploration.

Acknowledgements

TM is thankful for the initiation grant received from University of Southampton during the period of this research work. TM also acknowledges the grant received from Science and Engineering Research Board, India during the initial phase of this research.

Competing interests

The authors declare that they have no competing financial interests.

References

[1] D. Durbin, C. Malardier-Jugroot, Review of hydrogen storage techniques for on board vehicle applications, International Journal of Hydrogen Energy 38 (34) (2013) 14595–14617.

[2] I. Hassan, H. S. Ramadan, M. A. Saleh, D. Hissel, Hydrogen storage technologies for stationary and mobile applications: Review, analysis and perspectives, Renewable and Sustainable Energy Reviews 149 (2021) 111311.

[3] S. A. Sherif, F. Barbir, T. Veziroglu, Wind energy and the hydrogen economy—review of the technology, Solar energy 78 (5) (2005) 647–660.

[4] D. Haeseldonckx, W. D'haeseleer, The use of the natural-gas pipeline infrastructure for hydrogen transport in a changing market structure, International Journal of Hydrogen Energy 32 (10-11) (2007) 1381–1386.

[5] L. Schlapbach, A. Züttel, Hydrogen-storage materials for mobile applications, nature 414 (6861) (2001) 353–358.

[6] P. Sinha, T. Mukhopadhyay, Programmable multi-physical mechanics of mechanical metamaterials, Materials Science and Engineering: R: Reports 155 (2023) 100745.

[7] T. Ting, D. Barnett, Negative poisson's ratios in anisotropic linear elastic media, Journal of Applied Mechanics 76 (6) (2005) 929–931.

[8] G. N. Greaves, A. L. Greer, R. S. Lakes, T. Rouxel, Poisson's ratio and modern materials, Nature materials 10 (11) (2011) 823–837.

[9] T. Mukhopadhyay, J. Ma, H. Feng, D. Hou, J. M. Gattas, Y. Chen, Z. You, Programmable stiffness and shape modulation in origami materials: Emergence of a distant actuation feature, Applied Materials Today 19 (2020) 100537.

[10] T. Mukhopadhyay, S. Adhikari, A. Alu, Theoretical limits for negative elastic moduli in subacoustic lattice materials, Phys. Rev. B 99 (2019) 094108.

[11] B. Moura, M. Machado, T. Mukhopadhyay, S. Dey, Dynamic and wave propagation analysis of periodic smart beams coupled with resonant shunt circuits: Passive property modulation, Eur. Phys. J. Spec. Top. (accepted).

[12] A. Chaurha, P. Malaji, T. Mukhopadhyay, Dual functionality of vibration attenuation and energy harvesting: Effect of gradation on non-linear multi-resonator metastructures, The European Physical Journal Special Topics (accepted).

[13] L. Yongquiang, J. Zhiquiang, Free flexural vibration anlysis of symmetric rectangular honeycomb panels with scsc edge supports, Composite Structures 83 (2) (2008) 154 –158.

[14] T. Mukhopadhyay, S. Adhikari, Free vibration analysis of sandwich panels with randomly irregular honeycomb core, Journal of Engineering Mechanics 142 (11) (2016) 06016008.

[15] D. Zenkert, An Introduction to Sandwich Construction, Chameleon Press, London, 1995.

[16] F. Tornabene, M. Viscoti, R. Dimitri, M. A. Aiello, Higher order formulations for doubly-curved shell structures with a honeycomb core, Thin-Walled Structures 164 (2021) 107789.

[17] A. Bekele, M. A. Wadee, A. T. Phillips, Enhancing energy absorption through sequential instabilities in mechanical metamaterials, Royal Society Open Science 10 (8) (2023) 230762.

[18] N. A. Fleck, V. S. Deshpande, M. F. Ashby, Micro-architectured materials: past, present and future, Proceedings of the Royal Society A: Mathematical, Physical and Engineering Sciences 466 (2121) (2010) 2495–2516.

[19] A. A. Zadpoor, Mechanical meta-materials, Materials Horizons 3 (5) (2016) 371–381.

[20] T. Mukhopadhyay, S. Adhikari, A. Alu, Probing the frequency-dependent elastic moduli of lattice materials, Acta Materialia 165 (2019) 654–665.

[21] T. Van Manen, S. Janbaz, A. A. Zadpoor, Programming 2d/3d shape-shifting with hobbyist 3d printers, Materials horizons 4 (6) (2017) 1064–1069.

[22] Y. Chen, Z. Jia, L. Wang, Hierarchical honeycomb lattice metamaterials with improved thermal resistance and mechanical properties, Composite structures 152 (2016) 395–402.

[23] D. Zenkert, The handbook of sandwich construction, Engineering Materials Advisory Services, 1997.

[24] S. Malek, L. Gibson, Effective elastic properties of periodic hexagonal honeycombs, Mechanics of Materials 91 (2015) 226–240.

[25] F. Abd El-Sayed, R. Jones, I. Burgess, A theoretical approach to the deformation of honeycomb based composite materials, Composites 10 (4) (1979) 209–214.

[26] S. Balawi, J. Abot, The effect of honeycomb relative density on its effective in-plane elastic moduli: An experimental study, Composite Structures 84 (4) (2008) 293–299.

[27] M. Ryvkin, R. Shraga, Fracture toughness of hierarchical self-similar honeycombs, International Journal of Solids and Structures 152 (2018) 151–160.

[28] T. Thomas, G. Tiwari, Energy absorption and in-plane crushing behavior of aluminium reinforced honeycomb, Vacuum 166 (2019) 364–369.

[29] S. Adhikari, T. Mukhopadhyay, X. Liu, Broadband dynamic elastic moduli of honeycomb lattice materials: A generalized analytical approach, Mechanics of Materials 157 (2021) 103796.

[30] Y. Zhao, M. Ge, W. Ma, The effective in-plane elastic properties of hexagonal honeycombs with consideration for geometric nonlinearity, Composite Structures 234 (2020) 111749.

[31] L. J. Gibson, M. F. Ashby, Cellular solids: Structure and properties (1988).

[32] A. Wilbert, W.-Y. Jang, S. Kyriakides, J. Floccari, Buckling and progressive crushing of laterally loaded honeycomb, International Journal of Solids and Structures 48 (5) (2011) 803–816.

[33] W.-Y. Jang, S. Kyriakides, On the buckling and crushing of expanded honeycomb, International Journal of Mechanical Sciences 91 (2015) 81–90.

[34] S. Gonella, M. Ruzzene, Homogenization and equivalent in-plane properties of two-dimensional periodic lattices, International Journal of Solids and Structures 45 (10) (2008) 2897–2915.

[35] L. Hu, T. Yu, Mechanical behavior of hexagonal honeycombs under low-velocity impact–theory and simulations, International Journal of Solids and Structures 50 (20-21) (2013) 3152–3165.

[36] F. L. Jiménez, N. Triantafyllidis, Buckling of rectangular and hexagonal honeycomb under combined axial compression and transverse shear, International Journal of Solids and Structures 50 (24) (2013) 3934–3946.

[37] Q. Liu, Z. Mo, Y. Wu, J. Ma, G. C. P. Tsui, D. Hui, Crush response of cfrp square tube filled with aluminum honeycomb, Composites Part B: Engineering 98 (2016) 406–414.

[38] C. Zschernack, M. A. Wadee, C. Völlmecke, Nonlinear buckling of fibre-reinforced unit cells of lattice materials, Composite Structures 136 (2016) 217–228.

[39] F. Scarpa, P. Panayiotou, G. Tomlinson, Numerical and experimental uniaxial loading on in-plane auxetic honeycombs, The Journal of Strain Analysis for Engineering Design 35 (5) (2000) 383–388.

[40] T. Mukhopadhyay, S. Naskar, S. Adhikari, Anisotropy tailoring in geometrically isotropic multi-material lattices, Extreme Mechanics Letters 40 (2020) 100934.

[41] M. Awasthi, S. Naskar, A. Singh, T. Mukhopadhyay, Constitutive behavior of asymmetric multi-material honeycombs with bi-level variably-thickened composite architecture, Thin-Walled Structures 203 (2024) 112183.

[42] A. Bandyopadhyay, B. Heer, Additive manufacturing of multi-material structures, Materials Science and Engineering: R: Reports 129 (2018) 1–16.

[43] D. Chen, X. Zheng, Multi-material additive manufacturing of metamaterials with giant, tailorable negative poisson's ratios, Scientific reports 8 (1) (2018) 1–8.

[44] S. Tibbits, 4d printing: multi-material shape change, Architectural Design 84 (1) (2014) 116–121.

[45] T. Mukhopadhyay, S. Adhikari, Stochastic mechanics of metamaterials, Composite Structures 162 (2017) 85–97.

[46] T. Mukhopadhyay, S. Adhikari, Effective in-plane elastic moduli of quasi-random spatially irregular hexagonal lattices, International Journal of Engineering Science 119 (2017) 142–179.

[47] P. Sinha, T. Mukhopadhyay, Effective elastic properties of lattice materials with intrinsic stresses, Thin-Walled Structures 173 (2022) 108950.

[48] P. Prajwal, S. Ghuku, T. Mukhopadhyay, Large-deformation mechanics of anti-curvature lattice materials for mode-dependent enhancement of non-linear shear modulus, Mechanics of Materials 171 (2022) 104337.

[49] S. Ghuku, T. Mukhopadhyay, Anti-curvature honeycomb lattices for mode-dependent enhancement of nonlinear elastic properties under large deformation, International Journal of Non-Linear Mechanics 140 (2022) 103887.

[50] P. Tiwari, S. Naskar, T. Mukhopadhyay, Programmed out-of-plane curvature to enhance multi-modal stiffness of bending-dominated composite lattices, AIAA Journal 61 (4) (2023) 1820–1838.

[51] S. Ghuku, T. Mukhopadhyay, On enhancing mode-dependent failure strength under large deformation: The concept of anti-curvature in honeycomb lattices, Composite Structures 305 (2023) 116318.

[52] A. Singh, T. Mukhopadhyay, S. Adhikari, B. Bhattacharya, Extreme on-demand contactless mod-

ulation of elastic properties in magnetostrictive lattices, Smart Materials and Structures 31 (12) (2022) 125005.

[53] A. Singh, T. Mukhopadhyay, S. Adhikari, B. Bhattacharya, Active multi-physical modulation of poisson's ratios in composite piezoelectric lattices: on-demand sign reversal, Composite Structures 280 (2022) 114857.

[54] P. Sinha, T. Mukhopadhyay, On-demand contactless programming of nonlinear elastic moduli in hard magnetic soft beam based broadband active lattice materials, Smart Materials and Structures 32 (5) (2023) 055021.

[55] S. Mondal, T. Mukhopadhyay, S. Naskar, Active heterogeneous mode coupling in bi-level multi-physically architected metamaterials for temporal, on-demand and tunable programming, Communications Engineering (2024).

[56] P. Sinha, T. Mukhopadhyay, Pneumatic elastostatics of multi-functional inflatable lattices: realization of extreme specific stiffness with active modulation and deployability, Royal Society Open Science 11 (2) (2024) 231272.

[57] P. Tiwari, D. K. Maiti, D. Maity, Dynamic analysis of composite cylinders using 3-d degenerated shell elements, in: Recent Advances in Theoretical, Applied, Computational and Experimental Mechanics, Springer, 2020, pp. 261–276.

[58] A. Garg, H. Chalak, A review on analysis of laminated composite and sandwich structures under hygrothermal conditions, Thin-Walled Structures 142 (2019) 205–226.

[59] D. Delfosse, Fundamentals of functionally graded materials| s. suresh and a. mortensen iom communications ltd, 1998 isbn: 1-86125-063-0 (1998).

[60] L. L. Shaw, Thermal residual stresses in plates and coatings composed of multi-layered and functionally graded materials, Composites Part B: Engineering 29 (3) (1998) 199–210.

[61] M. Koizumi, Fgm activities in japan, Composites Part B: Engineering 28 (1-2) (1997) 1–4.

[62] J. Reddy, Analysis of functionally graded plates, International Journal for numerical methods in engineering 47 (1-3) (2000) 663–684.

[63] S. Abrate, Functionally graded plates behave like homogeneous plates, Composites part B: engineering 39 (1) (2008) 151–158.

[64] J. Woo, S. Meguid, L. Ong, Nonlinear free vibration behavior of functionally graded plates, Journal of sound and vibration 289 (3) (2006) 595–611.

[65] S. Ghuku, S. Sahoo, T. Mukhopadhyay, Nonlinear elasticity tailoring and failure mode manipulation of functionally graded honeycombs under large deformation, International Journal of Non-Linear

Mechanics 168 (2025) 104935.

[66] S. Ahmad, B. M. Irons, O. Zienkiewicz, Analysis of thick and thin shell structures by curved finite elements, International Journal for Numerical Methods in Engineering 2 (3) (1970) 419–451.

[67] S. Vlachoutsis, Explicit integration for three-dimensional degenerated shell finite elements, International journal for numerical methods in engineering 29 (4) (1990) 861–880.

[68] H. Huang, E. Hinton, A new nine node degenerated shell element with enhanced membrane and shear interpolation, International Journal for Numerical Methods in Engineering 22 (1) (1986) 73–92.

[69] W. K. Liu, E. Law, D. Lam, T. Belytschko, Resultant-stress degenerated-shell element, Computer Methods in Applied Mechanics and Engineering 55 (3) (1986) 259–300.

[70] A. Saleeb, T. Chang, W. Graf, A quadrilateral shell element using a mixed formulation, Computers & structures 26 (5) (1987) 787–803.

[71] S. Lee, S. Han, Free-vibration analysis of plates and shells with a nine-node assumed natural degenerated shell element, Journal of Sound and Vibration 241 (4) (2001) 605–633.

[72] P. Tiwari, S. K. Barman, D. K. Maiti, D. Maity, Free vibration analysis of delaminated composite plate using 3d degenerated element, Journal of Aerospace Engineering 32 (5) (2019) 04019070.

[73] P. K. Swain, P. Tiwari, D. K. Maiti, B. N. Singh, D. Maity, Active flutter control of delaminated composite plate using active fiber composite patches, Thin-Walled Structures 172 (2022) 108856.

[74] P. Tiwari, D. K. Maiti, D. Maity, 3-d sloshing of liquid filled laminated composite cylindrical tank under external excitation, Ocean Engineering 239 (2021) 109788.

[75] N. Sharma, P. Tiwari, D. K. Maiti, D. Maity, Free vibration analysis of functionally graded porous plate using 3-d degenerated shell element, Composites Part C: Open Access 6 (2021) 100208.

[76] Q. Li, Y. Qin, W. Gan, E. Li, L. Hu, L. Xu, Y. Guan, A filling lattice with actively controlled size/shape for energy absorption, International Journal of Mechanical Sciences 283 (2024) 109639.

[77] P. Sinha, D. Kundu, S. Naskar, T. Mukhopadhyay, Effective elastic properties of 3d lattice materials with intrinsic stresses: Bottom-up spectral characterization and constitutive programming, Applied Mathematical Modelling (2024) 115786.

[78] G. H. Loh, E. Pei, D. Harrison, M. D. Monzón, An overview of functionally graded additive manufacturing, Additive Manufacturing 23 (2018) 34–44.

[79] T. Beléndez, M. Pérez-Polo, C. Neipp, A. Beléndez, Numerical and experimental analysis of large deflections of cantilever beams under a combined load, Physica scripta 2005 (T118) (2005) 61.

[80] Y.-A. Kang, X.-F. Li, Bending of functionally graded cantilever beam with power-law non-linearity

subjected to an end force, International Journal of Non-Linear Mechanics 44 (6) (2009) 696–703.

[81] T.-A. Huynh, A.-T. Luu, J. Lee, Bending, buckling and free vibration analyses of functionally graded curved beams with variable curvatures using isogeometric approach, Meccanica 52 (2017) 2527–2546.

[82] B. Anirudh, T. B. Zineb, O. Polit, M. Ganapathi, G. Prateek, Nonlinear bending of porous curved beams reinforced by functionally graded nanocomposite graphene platelets applying an efficient shear flexible finite element approach, International Journal of Non-Linear Mechanics 119 (2020) 103346.

[83] Z.-H. Jin, R. Batra, R-curve and strength behavior of a functionally graded material, Materials Science and Engineering: A 242 (1-2) (1998) 70–76.